

---

# **Robust Attitude Control of Multirotor UAVs in the Presence of Parameter Uncertainties**

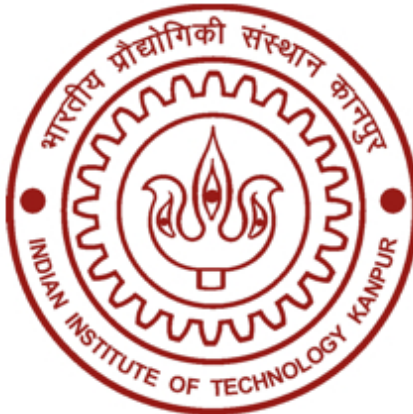
---

*A thesis submitted in fulfilment of the requirements*

*for the degree of Master of Technology*

*by*

Mahathi T. Bhargavapuri



DEPARTMENT OF ELECTRICAL ENGINEERING  
INDIAN INSTITUTE OF TECHNOLOGY KANPUR

June 2019

# Certificate

It is certified that the work contained in this thesis entitled **Robust Attitude Control of Multirotor UAVs in the Presence of Parameter Uncertainties** by **Mahathi T. Bhargavapuri** has been carried out under my supervision and that it has not been submitted elsewhere for a degree.

Soumya Ranjan Sahoo

*June 2019*

Assistant Professor

Department of Electrical Engineering

Indian Institute of Technology Kanpur

Mangal Kothari

*June 2019*

Associate Professor

Department of Aerospace Engineering

Indian Institute of Technology Kanpur

## Related Publications

M. Bhargavapuri, S. R. Sahoo, M. Kothari and Abhishek, “Robust Attitude Tracking in the Presence of Parameter Uncertainty for a Variable-Pitch Quadrotor”, in *Proceedings of the 2018 Annual American Control Conference (ACC)*, Milwaukee, WI, 2018, pp. 3454-3459. doi: [10.23919/ACC.2018.8431885](https://doi.org/10.23919/ACC.2018.8431885).

# *Abstract*

This thesis presents robust attitude control of multirotor unmanned aerial vehicles (UAVs). The use of multirotor UAVs for autonomous relief and reconnaissance missions has been widespread in recent years. Since the attitude dynamics of such multirotor UAVs are inherently unstable, attitude stabilization becomes necessary. However, the rotational inertia estimates of such UAVs are not always accurate and may even change during flight depending on the payload being carried. Controllers like PD, PI and PID are known to be robust to such uncertainties. However, existing works do not give a systematic way of determining the gains of such controllers to ensure robust stability in the presence of parametric uncertainties. The present work primarily focuses on developing a robust control law for the rigid body attitude dynamics of a multirotor and its implementation. The attitude dynamics is first linearized about the hover condition and a simple double integrator transfer function is obtained for the roll, pitch, and yaw subsystems. However, these transfer functions come with inverse multiplicative uncertainty due to rough rotational inertia estimates. A PD controller is implemented with a low-pass filter to stabilize the vehicle's attitude. Robustness to variation in parameters is incorporated and established using the robust stability criterion for SISO systems. Rotor dynamics for different types of multirotors (fixed-pitch and variable-pitch actuation) are discussed which provide useful insights about the control allocation problem. Using this knowledge in tandem with the robust attitude control design, lead compensators for quadrotors with fixed-pitch and variable-pitch propellers as well as a hexarotor with fixed-pitch propellers are implemented to demonstrate the modular nature of the design. Numerical simulations and experimental results validate the proposed control design and control allocation.

## *Acknowledgements*

I would like to take this opportunity to thank my supervisors Dr. Soumya Ranjan Sahoo and Dr. Mangal Kothari for their unwavering support throughout my life at IIT Kanpur both at academics and otherwise.

I would also like to thank all my lab mates and friends for helping me along this arduous journey and turning it into a bearable one. MV Ramana, C Vinodhini, Shridhar, and Arijit forming the original band when I joined IIT Kanpur. It was a great help during experiments to have Nidhish Raj and Ram D Gadekar along with their experience which deserves a lot of credit and appreciation. Dual degree guys made the experiments fun and I learned a lot from each of them - Jay, Hardik, Animesh, Harsh, and Ram.

I would also like to thank all my Music Club and Basketball team friends for molding me into someone different than the person who existed before entering IIT Kanpur.

Lastly, the campus is truly beautiful and provides a perfect setting to pursue anything that interests you and deserves a special acknowledgment.

# Contents

Certificate	i
Abstract	iii
Acknowledgements	iv
Contents	v
List of Figures	vii
List of Tables	x
Abbreviations	xi
Symbols	xii
<b>1 Introduction</b>	<b>1</b>
1.1 Conventional vs. Variable-Pitch Multicopters . . . . .	2
<b>2 Multicopter Rigid Body Dynamics</b>	<b>6</b>
2.1 Rotational Dynamics . . . . .	6
2.2 Translational Dynamics . . . . .	8
2.3 Rotor Dynamics . . . . .	9
2.3.1 Conventional Multicopters . . . . .	9
2.3.2 Variable-pitch Quadrotor . . . . .	9
2.4 Control Allocation . . . . .	10
2.4.1 Conventional Multicopters . . . . .	11
2.4.2 Variable-pitch Quadrotor . . . . .	14
<b>3 Robust Attitude Control Design</b>	<b>16</b>

3.1	Robust Controller for Roll Dynamics . . . . .	16
3.1.1	Robust Stability Analysis . . . . .	20
3.2	Control Synthesis . . . . .	21
3.2.1	Conventional Quadrotor . . . . .	21
3.2.2	Conventional Hexarotor . . . . .	25
3.2.3	Variable-pitch Quadrotor . . . . .	28
<b>4</b>	<b>Results</b>	<b>31</b>
4.1	Simulation Results . . . . .	31
4.1.1	Conventional Quadrotor . . . . .	32
4.1.2	Conventional Hexarotor . . . . .	36
4.1.3	Variable-pitch Quadrotor . . . . .	39
4.2	Experimental Results . . . . .	43
4.2.1	Conventional Quadrotor . . . . .	44
4.2.2	Conventional Hexarotor . . . . .	46
4.2.3	Variable-pitch Quadrotor . . . . .	48
<b>5</b>	<b>Concluding Remarks</b>	<b>51</b>
	<b>Bibliography</b>	<b>53</b>

# List of Figures

1.1	Actuation mechanisms in conventional and variable-pitch multirotors.	2
1.2	Conventional quadrotor and hexarotor used for experimental validation of the proposed control design methodology. . . . .	3
1.3	Variable-pitch quadrotor used for experiments. . . . .	4
2.1	Variable-pitch quadrotor. $\mathcal{F}_I$ indicates the inertial earth-fixed frame of reference and $\mathcal{F}_b$ indicates the body-fixed frame. . . . .	7
2.2	Nominal plant transfer function for roll dynamics. . . . .	8
2.3	Conventional quadrotor airframes with body-fixed frames indicated [1]. The $z_b$ -axes can be defined using the right hand rule. . . . .	12
2.4	Hexarotor airframes with body-fixed frames indicated [1]. The $z_b$ -axes can be defined using the right hand rule. . . . .	13
3.1	Roll dynamics with inverse multiplicative uncertainty. . . . .	17
3.2	Bode diagram for $G_0C(s)$ with the initial control design in (3.7) with $K_p = 0.35$ . . . . .	18
3.3	Bode diagram for $G_0C(s)$ with the modified control design in (3.8) with $K_p = 0.35$ . . . . .	19
3.4	Bode plot for roll subsystem $G_0C(s)$ with $K_p = 0.2$ for the quadrotor parameters given in Table 3.1 . . . . .	22
3.5	$ rS $ plot for roll subsystem for the quadrotor parameters given in Table 3.1 with $K_p = 0.2$ . The robust stability criterion is violated when the uncertainty is 90%, which is undesirable. . . . .	22
3.6	Modified bode plot for roll subsystem $G_0C(s)$ for the quadrotor parameters given in Table 3.1 . . . . .	23
3.7	$ rS $ plot for roll subsystem for the quadrotor parameters given in Table 3.1. The robust stability criterion is satisfied for both cases of uncertainty. . . . .	23
3.8	Bode plot for yaw subsystem for the quadrotor parameters given in Table 3.1 . . . . .	24
3.9	$ rS $ plot for yaw subsystem for the quadrotor parameters given in Table 3.1. Robust stability criterion is satisfied for $r = 0.7$ for both values of $\tau_d$ . . . . .	24

3.10	$ rS $ plot for yaw subsystem for the quadrotor parameters given in Table 3.1. Robust stability criterion is satisfied for $r = 0.9$ and $\tau_d = 0.002$ whereas it fails for $r = 0.9$ and $\tau_d = 0.02$ .	25
3.11	Bode plot based design for roll subsystem for the hexarotor parameters given in Table 3.2	26
3.12	$ rS $ plot for roll subsystem for the hexarotor parameters given in Table 3.2	27
3.13	Bode plot based design for yaw subsystem for the hexarotor parameters given in Table 3.2	27
3.14	$ rS $ plot for yaw subsystem for the hexarotor parameters given in Table 3.2.	28
3.15	$ rS $ plot for roll subsystem for the quadrotor parameters given in Table 3.3.	29
3.16	Bode plot based design for yaw subsystem for the quadrotor parameters given in Table 3.3	29
3.17	$ rS $ plot for yaw subsystem for the quadrotor parameters given in Table 3.3.	30
4.1	Roll angle tracking for a sinusoidal reference signal with amplitude $20^\circ$ and frequency 0.5 Hz. Parameters considered for the rigid-body dynamics simulations are given in Table 3.1.	32
4.2	Rotor speeds obtained using (2.12) for roll tracking in Fig. 4.1.	33
4.3	Roll angle tracking for a sinusoidal reference signal with amplitude $20^\circ$ and frequency 0.5 Hz. Parameters considered for the rigid-body dynamics simulations are 70% deviated from those given in Table 3.1 which creates an uncertainty of $r = 0.7$ .	33
4.4	Rotor speeds obtained using (2.12) for roll tracking in Fig. 4.3.	34
4.5	Roll angle tracking for a sinusoidal reference signal with amplitude $20^\circ$ and frequency 2 Hz. Parameters considered for the rigid-body dynamics simulations are same as those given in Table 3.1.	35
4.6	Rotor speeds obtained using (2.12) for roll tracking in Fig. 4.5.	35
4.7	Roll angle tracking for a sinusoidal reference signal with amplitude $20^\circ$ and frequency 0.5 Hz. Parameters considered for the rigid-body dynamics simulations are given in Table 3.2.	36
4.8	Rotor speeds obtained using (2.18) for roll tracking in Fig. 4.7.	37
4.9	Roll angle tracking for a sinusoidal reference signal with amplitude $20^\circ$ and frequency 0.5 Hz. Parameters considered for the rigid-body dynamics simulations are 70% deviated from those given in Table 3.2 which creates an uncertainty of $r = 0.7$ .	37
4.10	Rotor speeds obtained using (2.18) for roll tracking in Fig. 4.9.	38
4.11	Roll angle tracking for a sinusoidal reference signal with amplitude $20^\circ$ and frequency 2 Hz. Parameters considered for the rigid-body dynamics simulations are given in Table 3.2.	38

4.12 Rotor speeds obtained using (2.18) for roll tracking in Fig. 4.11. . . . .	39
4.13 Roll angle tracking for a sinusoidal reference signal with amplitude 20° and frequency 0.5 Hz. Parameters considered for the rigid-body dynamics simulations are identical to those given in Table 3.3. . . . .	40
4.14 Trust coefficients (virtual controls) and collective blade pitch angles (actuators) for roll tracking in Fig. 4.13. . . . .	40
4.15 Roll angle tracking for a sinusoidal reference signal with amplitude 20° and frequency 0.5 Hz. Parameters considered for the rigid-body dynamics simulations are 70% deviated from those given in Table 3.3. . . . .	41
4.16 Trust coefficients (virtual controls) and collective blade pitch angles (actuators) for roll tracking in Fig. 4.15. . . . .	41
4.17 Roll angle tracking for a sinusoidal reference signal with amplitude 20° and frequency 0.5 Hz. Parameters considered for the rigid-body dynamics simulations are identical to those given in Table 3.3. . . . .	42
4.18 Trust coefficients (virtual controls) and collective blade pitch angles (actuators) for roll tracking in Fig. 4.17. . . . .	42
4.19 Conventional quadrotor in hover condition. . . . .	44
4.20 Roll, pitch, and yaw tracking using the conventional quadrotor in Fig. 1.2 (A). The compensator synthesized in Fig. 3.6 is used for the roll and pitch tracking for this vehicle. The compensator synthesized in Fig. 3.8 is used for yaw subsystem control. . . . .	45
4.21 Screen grabs of the conventional quadrotor during test flights. . . . .	45
4.22 Screen grabs of the conventional quadrotor performing pitch up and down maneuvers. . . . .	46
4.23 Conventional hexarotor in hover state. . . . .	46
4.24 Roll, pitch, and yaw tracking using the variable-pitch quadrotor in Fig. 1.2 (B). The compensator synthesized in Fig. 3.11 is used for the roll and pitch tracking for this vehicle. The compensator synthesized in Fig. 3.13 is used for yaw subsystem control. . . . .	47
4.25 Screen grabs of the conventional hexarotor during test flights. . . . .	47
4.26 Screen grabs of the conventional hexarotor performing pitching moment maneuvers. . . . .	48
4.27 Variable-pitch quadrotor in hover state. . . . .	48
4.28 Roll, pitch, and yaw tracking using the variable-pitch quadrotor in Fig. 1.3. The compensator synthesized in Fig. 3.3 is used for the roll and pitch tracking for this vehicle. The compensator synthesized in Fig. 3.16 is used for yaw subsystem control. . . . .	49
4.29 Screen grabs of the variable-pitch quadrotor during test flights. . . . .	49
4.30 Screen grabs of the variable-pitch quadrotor performing negative and positive roll maneuvers. . . . .	50

# List of Tables

3.1	Parameters for the conventional quadrotor. . . . .	21
3.2	Parameters for the conventional hexarotor. . . . .	25
3.3	Parameters for the variable-pitch quadrotor. . . . .	28

# Abbreviations

<b>UAV</b>	Unmanned Aerial Vehicle
<b>VTOL</b>	Vertical Take Off and Landing
<b>PD</b>	Proportional Derivative
<b>LQ</b>	Linear Quadratic
<b>PI</b>	Proportional Integral
<b>PID</b>	Proportional Integral Derivative
<b>PM</b>	Phase Margin
<b>DoF</b>	Degree(s) of Freedom

# Symbols

$\rho$	Density of air at mean sea level, in $\text{kg m}^{-3}$ .
$\phi, \theta, \psi$	Euler angles, in rad.
$\theta_0$	Collective blade pitch angle, in rad.
$\sigma$	Solidity ratio.
$\Omega$	Rotor angular speed, in $\text{rad s}^{-1}$ .
$\tau_d$	Time constant of first-order low-pass filter, in s.
$c$	Chord length of the rotor blade, in m.
$C_{d0}$	Zero lift drag coefficient.
$C_{l\alpha}$	Airfoil lift curve slope, in $\text{rad}^{-1}$ .
$C_T$	Thrust coefficient.
$C_Q$	Torque coefficient.
$\mathcal{F}_b$	The body-fixed frame of reference.
$\mathcal{F}_I$	The earth-fixed (inertial) frame of reference.
$g$	Acceleration due to earth's gravity, in $\text{m s}^{-2}$ .
$I_{xx}, I_{yy}, I_{zz}$	Rotational inertia about the body-fixed $x_b$ -, $y_b$ - and $z_b$ -axes, respectively, in $\text{kg m}^2$ .
$k$	Control allocation gain.
$k_f$	Force coefficient, in $\text{N s}^2/\text{rad}^2$ .
$k_m$	Moment coefficient, in $\text{N m s}^2/\text{rad}^2$ .
$K_p$	Proportional gain.
$K_d$	Derivative gain.
$L$	Rolling moment input, in N m.

$M$	Pitching moment input, in N m.
$m$	Mass of the UAV, in kg.
$N$	Yawing moment input, in N m.
$N_b$	Number of blades present in a rotor.
$p, q, r$	Angular velocities about the body-fixed $x_b$ -, $y_b$ - and $z_b$ -axes, respectively, in rad s <sup>-1</sup> .
$Q_i$	Drag torque produced by the $i^{\text{th}}$ rotor, in N m.
$R$	Rotor radius, in m.
$S$	Sensitivity function.
$T$	Total thrust input, in N.
$T_i$	Thrust generated by the $i^{\text{th}}$ rotor, in N.
$x, y, z$	Position of the UAV's center of mass in the earth-fixed frame.

*Dedicated to my Parents and Gurus.*

# Chapter 1

## Introduction

Quadrrotors have been at the heart of much of the research on unmanned aerial vehicles (UAVs) with vertical take-off and landing (VTOL) capabilities. Their mechanical simplicity allows assembly and usage in a straightforward fashion. For such vehicles, actuator performance is the limiting factor and not the control law used [2]. Hence, the nonlinear attitude dynamics can be linearized about the hover condition and traditional PD controllers are designed for attitude stabilization and tracking. This also offers robustness to parameter variation and modeling uncertainties.

Various control techniques have been applied successfully on conventional quadrotor UAVs. Model based control design such as dynamic inversion [3], feedback linearization [4], and backstepping [5, 6] are popular nonlinear techniques to achieve full quadrotor control. However, there is a need for accurate vehicle modeling in the aforementioned control laws. Controllers which are robust to model uncertainties use sliding mode techniques [7, 8]. But implementing this on actuators with dynamics of their own may induce chattering. Linearized models have been derived in [9] and used to design adaptive control law for fault tolerance. Linear controllers [10, 11] have been used extensively to stabilize attitude dynamics, but no systematic analysis to arrive at the gains has been discussed.

In this work, a lead compensator-type design is used for attitude stabilization. A simple PD controller is not implementable to the absence of poles in such a controller. Hence, a lead compensator-type design is chosen. This also enables us to place the pole of the controller in such a way that maximum possible bandwidth

can be obtained while cutting off high frequency noise. The controller structure is manipulated using the knowledge of attitude and angular rate dynamics so that only one tuning parameter is required. This parameter or “gain” is tuned in such a way that the robust stability criterion is always satisfied for a given amount of rotational inertia uncertainty. To show the effectiveness of the proposed compensator, rough estimates of the rotational inertia of the rigid body are used. The lead compensator is implemented on both conventional and variable-pitch multirotor UAVs to show the simplicity of design and its modularity.

## 1.1 Conventional vs. Variable-Pitch Multicopters

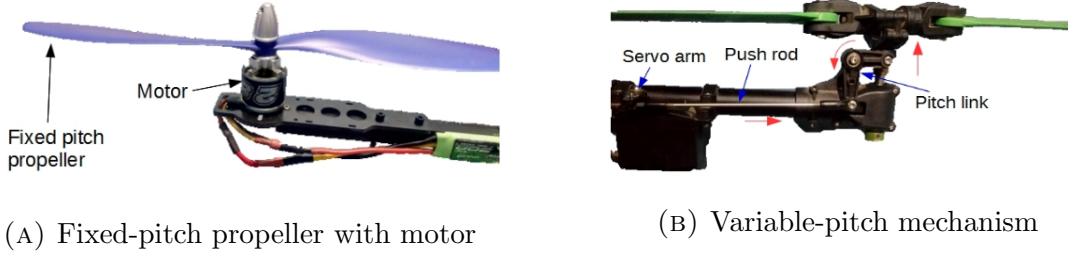
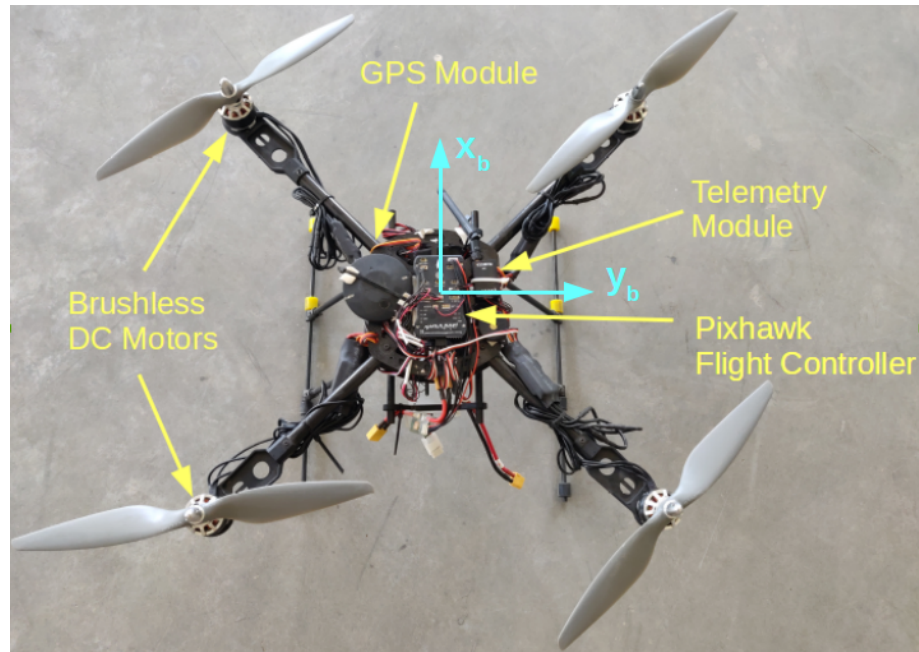
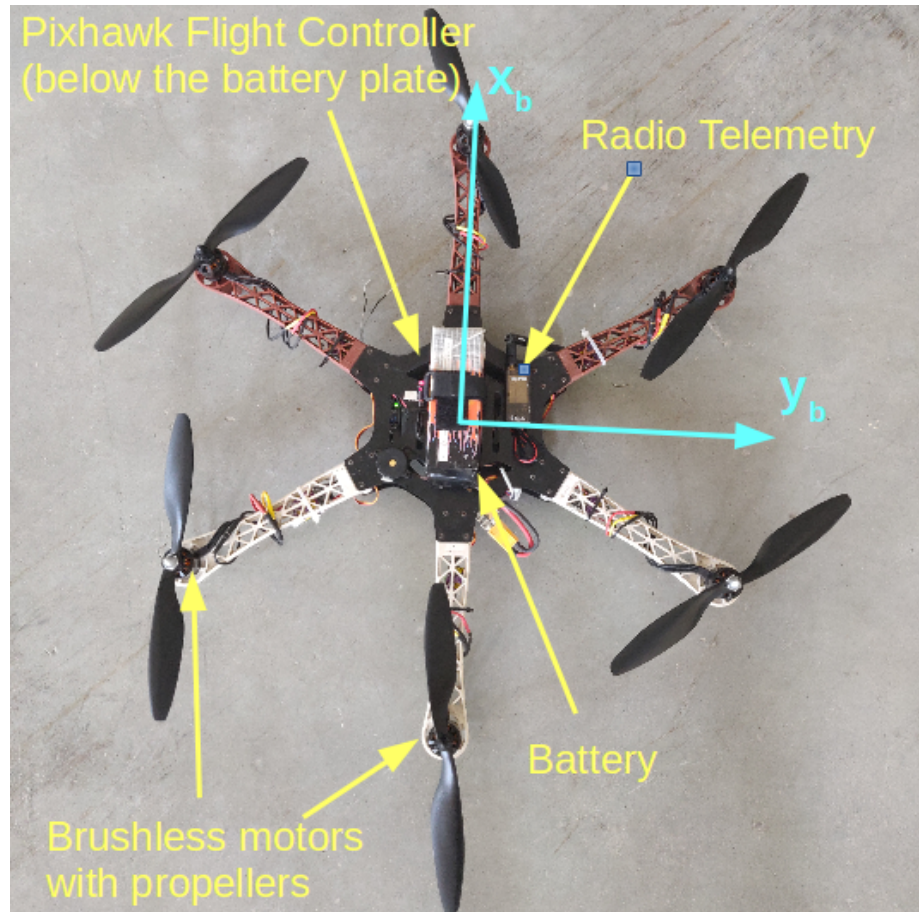


FIGURE 1.1: Actuation mechanisms in conventional and variable-pitch multicopters.

One of the main aims of this work is to demonstrate its applicability to a wide class of multicopters. The proposed robust attitude controller can be used with any multicopter with only a rough estimate of its inertia and knowledge of its rotor dynamics. This is shown through a systematic control design process which is then applied to both conventional and variable-pitch quadrotors. In this work, the term multicopter and quadrotor are used interchangeably. This is due to the fact that quadrotors form a subset of multicopters and the only differentiating quality between quadrotors and the remaining elements of this larger set becomes the number of rotors. Multicopters with more than four rotors are used to obtain larger lifting capability as well as redundancy in actuation. Fewer than four rotors changes actuator dynamics for the yaw subsystem. However, the same control design methodology can be used in all the above cases. This is verified by implementing the proposed control law on a hexarotor UAV.



(A) Conventional quadrotor



(B) Conventional hexarotor

FIGURE 1.2: Conventional quadrotor and hexarotor used for experimental validation of the proposed control design methodology.

The amount of lift produced by a rotor is controlled by either changing the angular speed of the rotor or the collective blade pitch angle. Conventional multirotors use the former while variable-pitch, as the name suggests, uses the latter form of actuation. The actuation mechanism for both cases is shown in Fig. 1.1. The problem with fixed-pitch, variable-speed actuation is that its response is limited by the rotational inertia of the motor used. While this type of actuation works satisfactorily for small-scale UAVs, it becomes a serious constraint on the vehicle's overall size and lifting capacity. A comparison between fixed and variable-pitch thrust actuation has been carried out by Cutler et al. [12]. Variable-pitch propellers have faster thrust actuation and can be powered by a single power plant. This implies larger quadrotors with gasoline engines can be fashioned with higher endurance and payload carrying capacity [13]. However, this type of quadrotor introduces new challenges. One such problem is instability caused by vibrations and high frequency noise. Uncertainty in parameters also causes various problems during control design and implementation. The proposed attitude controller is shown to be robust to such disturbances and uncertainties through rigorous numerical simulations and experiments on both conventional and variable-pitch multirotors. The vehicles used for experiments are shown in Fig. 1.2 and 1.3.

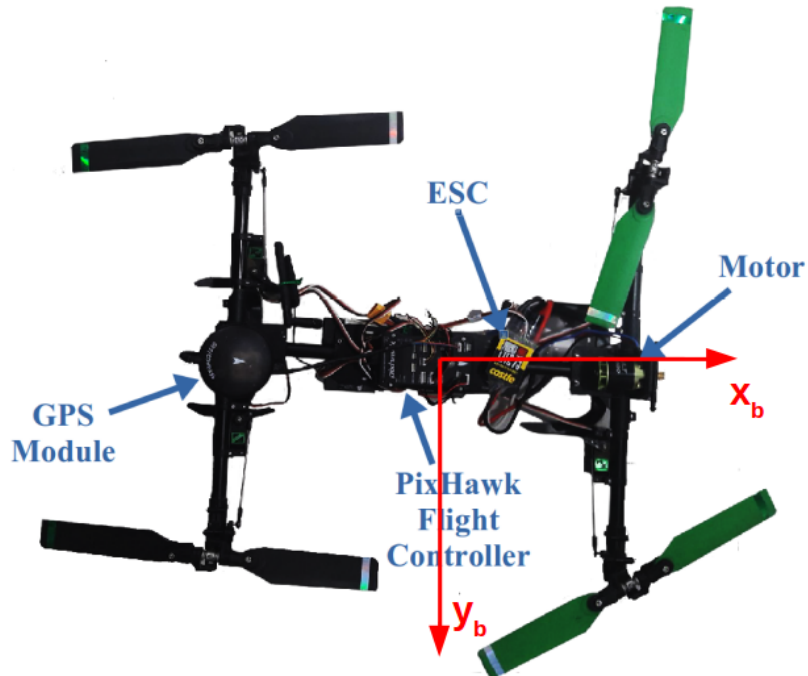


FIGURE 1.3: Variable-pitch quadrotor used for experiments.

Literature on control for variable-pitch quadrotors is limited and robustness analysis has seldom been carried out. Nonlinear control using dynamic inversion has been simulated for a variable-pitch quadrotor in [14]. However, the control methodology used is very sensitive to modeling inaccuracies. In this work, we consider large uncertainties in rotational inertia estimates, and design a lead compensator which satisfies the criterion for robust stability. A low-pass filter is used to reject high frequency jitters due to derivative action. A control allocation step ensures that the actual control inputs reach their desired values (generated by controller). The compensator is validated through extensive simulations and experiments.

# Chapter 2

## Multirotor Rigid Body Dynamics

This chapter introduces the rigid body dynamics of a multirotor UAV derived using linear and angular momentum conservation laws. Since this work deals with robust control for the attitude subsystem, only the angular kinematics and dynamics are described in detail. Translational dynamics are provided for completeness. A separate section on rotor dynamics discusses the two possible types of actuation and the associated dynamics. This enables us to better understand and derive control allocation for both types of multicopters, viz.: fixed-pitch (conventional) and variable-pitch multicopters.

### 2.1 Rotational Dynamics

In this section, a simple linearized model for the rotational dynamics of a multirotor UAV is presented. The system is linearized about hover condition. For small deviations from hover, it is assumed that the following approximation holds:

$$p = \dot{\phi}, \ q = \dot{\theta}, \ r = \dot{\psi}, \quad (2.1)$$

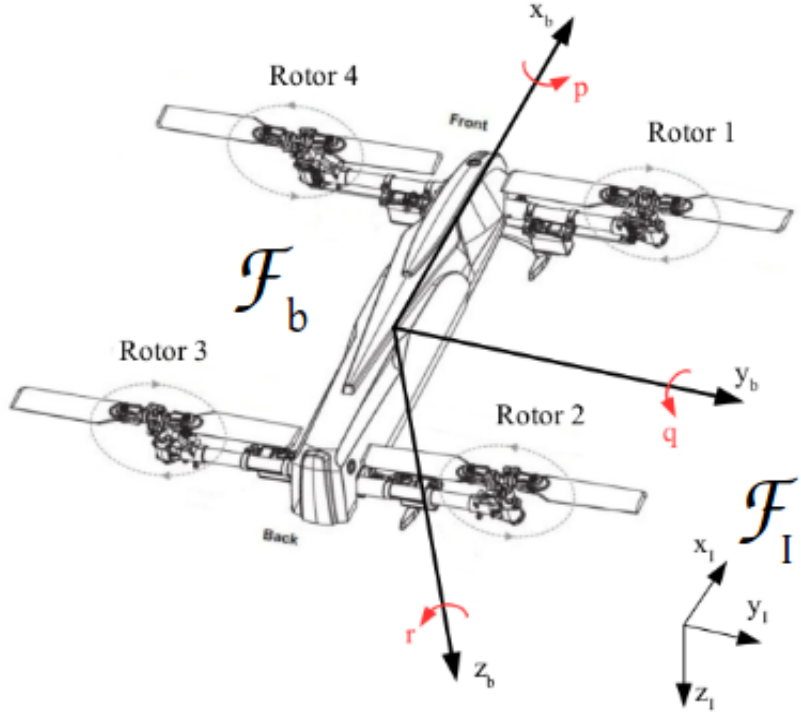


FIGURE 2.1: Variable-pitch quadrotor.  $\mathcal{F}_I$  indicates the inertial earth-fixed frame of reference and  $\mathcal{F}_b$  indicates the body-fixed frame.

The full dynamic model is given by

$$\ddot{\phi} = \frac{I_{yy} - I_{zz}}{I_{xx}} \dot{\theta} \dot{\psi} + \frac{L}{I_{xx}}, \quad (2.2a)$$

$$\ddot{\theta} = \frac{I_{zz} - I_{xx}}{I_{yy}} \dot{\phi} \dot{\psi} + \frac{M}{I_{yy}}, \quad (2.2b)$$

$$\ddot{\psi} = \frac{I_{xx} - I_{yy}}{I_{zz}} \dot{\phi} \dot{\theta} + \frac{N}{I_{zz}}, \quad (2.2c)$$

where  $\phi$  (roll),  $\theta$  (pitch), and  $\psi$  (yaw) are Euler angles,  $I_{xx}$ ,  $I_{yy}$ , and  $I_{zz}$  are the diagonal terms in the inertia matrix, and  $L$ ,  $M$ , and  $N$  are moment inputs in the body-fixed frame. Neglecting higher order terms and linearizing the rotational dynamics in (2.2), we get

$$\ddot{\phi} = \frac{L}{I_{xx}}; \quad \ddot{\theta} = \frac{M}{I_{yy}}; \quad \ddot{\psi} = \frac{N}{I_{zz}}. \quad (2.3)$$

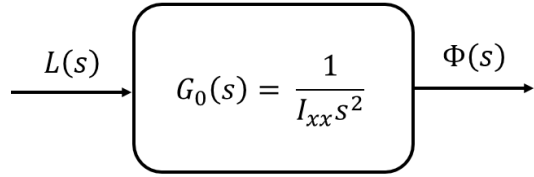


FIGURE 2.2: Nominal plant transfer function for roll dynamics.

Linearization about hover dynamics leads to decoupling of roll, pitch, and yaw dynamics. These decoupled dynamics can be used to create transfer function models in the Laplace domain for individual subsystems. The subsystem for roll dynamics is shown in Fig. 2.2. Similar subsystems can be created for pitch and yaw dynamics. Since the inertia parameters  $I_{xx}$ ,  $I_{yy}$ , and  $I_{zz}$  may not be known exactly, we aim at designing a robust PD controller for the rotational dynamics. Next, we describe the translational dynamics for the vehicle.

## 2.2 Translational Dynamics

The translational dynamics of a multirotor UAV can be derived using Newton's laws of motion [5, 15]. This is given by

$$\begin{pmatrix} \ddot{x} \\ \ddot{y} \\ \ddot{z} \end{pmatrix} = \begin{pmatrix} 0 \\ 0 \\ g \end{pmatrix} - \frac{T}{m} \begin{pmatrix} \cos \phi \sin \theta \cos \psi + \sin \phi \sin \psi \\ \cos \phi \sin \theta \sin \psi - \sin \phi \cos \psi \\ \cos \phi \cos \theta \end{pmatrix}, \quad (2.4)$$

where  $(x, y, z)$  is the position in the earth-fixed frame of reference,  $T$  is the total thrust provided by the rotors,  $m$  is the mass of the quadrotor, and  $g$  is the acceleration due to gravity. The acceleration term  $\frac{T}{m}$  is defined in the body-fixed frame and is transformed into the earth-fixed frame through the Euler angle sequence 3-2-1 ( $\psi$ - $\theta$ - $\phi$ ) [16]. The error in estimation of mass of the vehicle is negligible compared to inertia parameter estimates. Hence, robustness analysis for translational dynamics is skipped in this work.

## 2.3 Rotor Dynamics

The moments and thrust required to control the rotational and translational dynamics of a multirotor are generated by varying the thrust and torque produced by individual rotors. The thrust and torque generated by the  $i^{\text{th}}$  rotor are given by

$$\begin{aligned} T_i &= C_{T_i} \rho \pi R_i^2 V_{i \text{ tip}}^2 \\ Q_i &= R_i C_{Q_i} \rho \pi R_i^2 V_{i \text{ tip}}^2, \end{aligned} \quad (2.5)$$

where  $C_T$  is the thrust coefficient,  $C_Q$  is the torque coefficient,  $\rho$  is the density of air,  $R$  is the rotor radius,  $V_{\text{tip}} = \Omega R$ , and  $\Omega$  is angular speed of the rotor. From (2.5), we observe that the thrust and torque produced by the  $i^{\text{th}}$  rotor can be controlled by varying either the rotor angular speed or the thrust/torque coefficient.

### 2.3.1 Conventional Multicopters

In conventional multirotor UAVs, the thrust and torque produced by each rotor is controlled by varying the angular speed of the rotor while keeping the remaining variables on the right hand side of (2.5) constant. Hence, (2.5) can be rewritten as

$$\begin{aligned} T_i &= k_f \Omega_i^2 \\ Q_i &= k_m \Omega_i^2 \end{aligned} \quad (2.6)$$

where  $k_f$  is the force coefficient and  $k_m$  is the moment coefficient of the rotor. Note that the coefficients  $C_T$  and  $C_Q$  are non-dimensional quantities whereas  $k_f$  and  $k_m$  are not.

### 2.3.2 Variable-pitch Quadrotor

Unlike a conventional multirotor, the thrust produced by each rotor of a variable-pitch quadrotor is varied by changing collective pitch of the rotor blades. The relationship between collective pitch angle ( $\theta_0$ ), thrust coefficient ( $C_T$ ), and torque

coefficient ( $C_Q$ ) is given by

$$\theta_0 = \frac{6C_T}{\sigma C_{l_\alpha}} + \frac{3}{2} \sqrt{\frac{C_T}{2}}, \quad (2.7)$$

$$C_Q = \frac{1}{2}\sigma \left( \frac{\sqrt{2}C_T^{\frac{3}{2}}}{\sigma} + \frac{C_{d_0}}{4} \right), \quad (2.8)$$

where  $\sigma = \frac{N_b c}{\pi R}$  is the solidity ratio,  $c$  is the chord length of the blade,  $N_b$  is the number of blades,  $C_{l_\alpha}$  is the airfoil lift curve slope, and  $C_{d_0}$  is the zero lift drag coefficient of the airfoil. Note that the thrust coefficient is always positive and only the positive root is considered for computation of collective pitch angle and torque coefficient. The thrust and torque produced by the  $i^{th}$  rotor can be expressed as

$$\begin{aligned} T_i &= KC_{T_i} \\ Q_i &= KRC_{Q_i}, \end{aligned} \quad (2.9)$$

where  $K = \rho\pi R^2 V_{tip}^2$ .  $K$  is typically a constant since  $\Omega$  is regulated about a constant value. Detailed derivation of (2.7), (2.8), and (2.9) can be found in [17]. The thrust and torque coefficients can be used as virtual control inputs and design control allocation for the variable-pitch quadrotor utilizing these coefficients [14]. This is given in detail in the next section.

## 2.4 Control Allocation

From (2.6) and (2.9), we observe that control allocation for conventional multirotors and variable-pitch quadrotors has to be carried out separately. Even though control allocation for both types of vehicles is well documented in literature, it is presented here for completeness.

### 2.4.1 Conventional Multirotors

Control allocation for conventional multirotors is simple, straightforward, and hence well documented [15, 18]. In this work, control allocation for quadrotors and hexarotors are given for two different configurations each. This allows us to employ the robust attitude control design for multiple types of multirotor UAVs.

The control inputs  $T$ ,  $L$ ,  $M$ , and  $N$  (in the body-fixed frame) are allocated to the rotors using (2.6). For a quadrotor in X-configuration (see Fig. 2.3(a)), the control signals are generated by

$$\begin{aligned} T &= k_f(\Omega_1^2 + \Omega_2^2 + \Omega_3^2 + \Omega_4^2) \\ L &= d k_f(-\Omega_1^2 + \Omega_2^2 + \Omega_3^2 - \Omega_4^2) \\ M &= d k_f(\Omega_1^2 - \Omega_2^2 + \Omega_3^2 - \Omega_4^2) \\ N &= k_m(\Omega_1^2 + \Omega_2^2 - \Omega_3^2 - \Omega_4^2) \end{aligned} \quad (2.10)$$

where  $d$  is the distance between the rotor axis and the vehicle's center of gravity. To obtain the rotor speeds from the  $T$ ,  $L$ ,  $M$ , and  $N$  generated by the position and attitude controllers, the  $4 \times 4$  matrix formed using (2.10) can be inverted since all its entries are positive real numbers and is invertible. For greater clarity, (2.10) is written in vector form as follows:

$$\begin{bmatrix} T \\ L \\ M \\ N \end{bmatrix} = \begin{bmatrix} k_f & k_f & k_f & k_f \\ -d k_f & d k_f & d k_f & -d k_f \\ d k_f & -d k_f & d k_f & -d k_f \\ k_m & k_m & -k_m & -k_m \end{bmatrix} \begin{bmatrix} \Omega_1^2 \\ \Omega_2^2 \\ \Omega_3^2 \\ \Omega_4^2 \end{bmatrix} \quad (2.11)$$

However, inverting the  $4 \times 4$  matrix in (2.11) becomes challenging due to numerical constraints. Such numerical constraints arise since values of  $k_f$  and  $k_m$  are of the order  $10^{-5}$  or smaller. To simplify the process of obtaining rotor speeds without inverting matrices (it becomes non-square in the case of hexa- and octa-rotors), an

allocation matrix is created as follows:

$$\begin{bmatrix} \Omega_1^2 \\ \Omega_2^2 \\ \Omega_3^2 \\ \Omega_4^2 \end{bmatrix} = \frac{1}{4} \begin{bmatrix} 1/k_f & -1/(d k_f) & 1/(d k_f) & 1/k_m \\ 1/k_f & 1/(d k_f) & -1/(d k_f) & 1/k_m \\ 1/k_f & 1/(d k_f) & 1/(d k_f) & -1/k_m \\ 1/k_f & -1/(d k_f) & -1/(d k_f) & -1/k_m \end{bmatrix} \begin{bmatrix} T \\ L \\ M \\ N \end{bmatrix} \quad (2.12)$$

This eliminates the need for matrix inversion to obtain rotor speeds. Similarly, the control signals for a quadrotor in +-configuration are generated by

$$\begin{aligned} T &= k_f(\Omega_1^2 + \Omega_2^2 + \Omega_3^2 + \Omega_4^2) \\ L &= d k_f(-\Omega_1^2 + \Omega_2^2) \\ M &= d k_f(\Omega_3^2 - \Omega_4^2) \\ N &= k_m(\Omega_1^2 + \Omega_2^2 - \Omega_3^2 - \Omega_4^2) \end{aligned} \quad (2.13)$$

and the rotor speed allocation is obtained by

$$\begin{bmatrix} \Omega_1^2 \\ \Omega_2^2 \\ \Omega_3^2 \\ \Omega_4^2 \end{bmatrix} = \frac{1}{4} \begin{bmatrix} 1/k_f & -1/(d k_f) & 0 & 1/k_m \\ 1/k_f & 1/(d k_f) & 0 & 1/k_m \\ 1/k_f & 0 & 1/(d k_f) & -1/k_m \\ 1/k_f & 0 & -1/(d k_f) & -1/k_m \end{bmatrix} \begin{bmatrix} T \\ L \\ M \\ N \end{bmatrix} \quad (2.14)$$

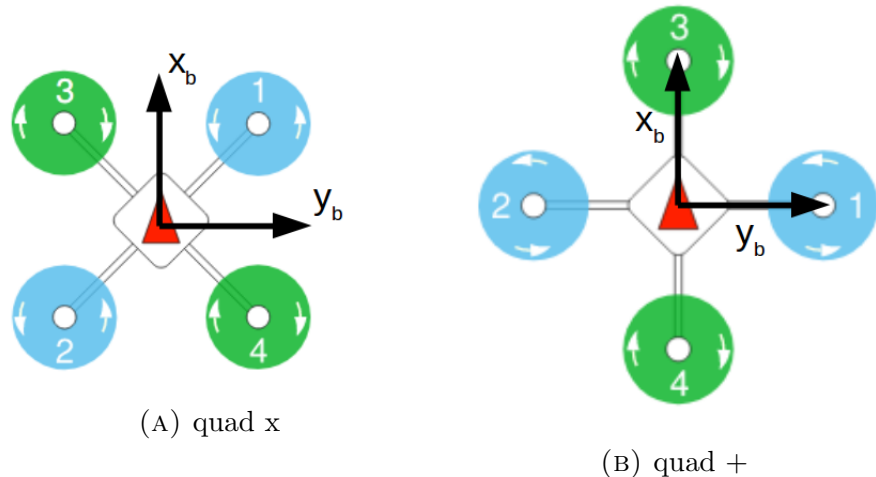


FIGURE 2.3: Conventional quadrotor airframes with body-fixed frames indicated [1]. The  $z_b$ -axes can be defined using the right hand rule.

This idea of control allocation for conventional multirotors can be extended to any other air frame [1] whose thrust and torque are varied using (2.6). To demonstrate this, we use the example of hexarotor in both X- and +-configurations (Fig. 2.4). The control inputs are generated for a hexarotor in X-configuration as follows:

$$\begin{aligned} T &= k_f(\Omega_1^2 + \Omega_2^2 + \Omega_3^2 + \Omega_4^2 + \Omega_5^2 + \Omega_6^2) \\ L &= d k_f(-\Omega_1^2 + \Omega_2^2 + \Omega_3^2 - \Omega_4^2 - \Omega_5^2 + \Omega_6^2) \\ M &= d k_f(\Omega_3^2 - \Omega_4^2 + \Omega_5^2 - \Omega_6^2) \\ N &= k_m(-\Omega_1^2 + \Omega_2^2 - \Omega_3^2 + \Omega_4^2 + \Omega_5^2 - \Omega_6^2) \end{aligned} \quad (2.15)$$

Using the idea in (2.12) to allocate rotor speeds for hexarotors without matrix inversion (note that here the matrix is non-square), we get

$$\begin{bmatrix} \Omega_1^2 \\ \Omega_2^2 \\ \Omega_3^2 \\ \Omega_4^2 \\ \Omega_5^2 \\ \Omega_6^2 \end{bmatrix} = \frac{1}{6} \begin{bmatrix} 1/k_f & -1/(d k_f) & 0 & -1/k_m \\ 1/k_f & 1/(d k_f) & 0 & 1/k_m \\ 1/k_f & 1/(d k_f) & 1/(d k_f) & -1/k_m \\ 1/k_f & -1/(d k_f) & -1/(d k_f) & 1/k_m \\ 1/k_f & -1/(d k_f) & 1/(d k_f) & 1/k_m \\ 1/k_f & 1/(d k_f) & -1/(d k_f) & -1/k_m \end{bmatrix} \begin{bmatrix} T \\ L \\ M \\ N \end{bmatrix} \quad (2.16)$$

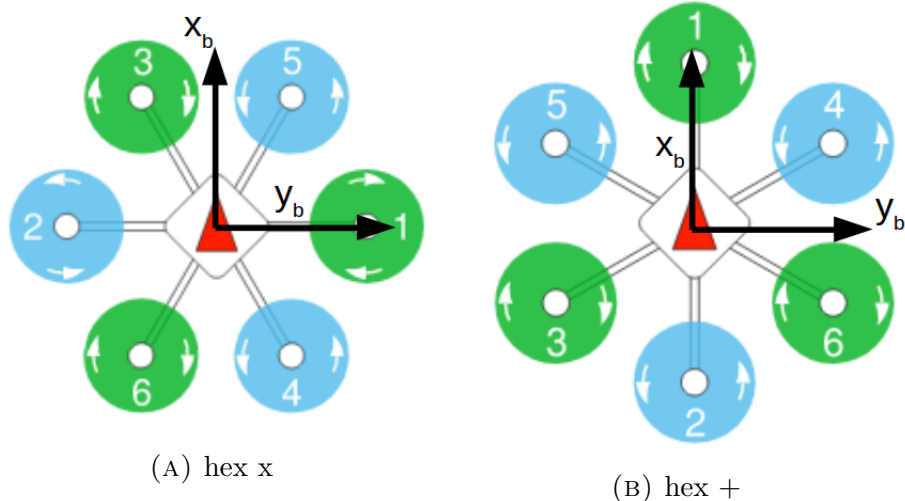


FIGURE 2.4: Hexarotor airframes with body-fixed frames indicated [1]. The  $z_b$ -axes can be defined using the right hand rule.

The control inputs for a hexarotor in +-configuration are generated by

$$\begin{aligned} T &= k_f(\Omega_1^2 + \Omega_2^2 + \Omega_3^2 + \Omega_4^2 + \Omega_5^2 + \Omega_6^2) \\ L &= d k_f(\Omega_3^2 - \Omega_4^2 + \Omega_5^2 - \Omega_6^2) \\ M &= d k_f(\Omega_1^2 - \Omega_2^2 - \Omega_3^2 + \Omega_4^2 + \Omega_5^2 - \Omega_6^2) \\ N &= k_m(-\Omega_1^2 + \Omega_2^2 - \Omega_3^2 + \Omega_4^2 + \Omega_5^2 - \Omega_6^2) \end{aligned} \quad (2.17)$$

and the rotor speeds can be obtained by

$$\begin{bmatrix} \Omega_1^2 \\ \Omega_2^2 \\ \Omega_3^2 \\ \Omega_4^2 \\ \Omega_5^2 \\ \Omega_6^2 \end{bmatrix} = \frac{1}{6} \begin{bmatrix} 1/k_f & 0 & 1/(d k_f) & -1/k_m \\ 1/k_f & 0 & -1/(d k_f) & 1/k_m \\ 1/k_f & 1/(d k_f) & -1/(d k_f) & -1/k_m \\ 1/k_f & -1/(d k_f) & 1/(d k_f) & 1/k_m \\ 1/k_f & 1/(d k_f) & 1/(d k_f) & 1/k_m \\ 1/k_f & -1/(d k_f) & -1/(d k_f) & -1/k_m \end{bmatrix} \begin{bmatrix} T \\ L \\ M \\ N \end{bmatrix} \quad (2.18)$$

### 2.4.2 Variable-pitch Quadrotor

The control allocation for a variable-pitch quadrotor is different from that of conventional multirotors since it is based on (2.9) rather than (2.5). The control inputs  $T$ ,  $L$ ,  $M$ , and  $N$  (in the body-fixed frame as shown in Fig. 2.1) for a variable-pitch quadrotor are given by

$$\begin{aligned} T &= K(C_{T_1} + C_{T_2} + C_{T_3} + C_{T_4}) \\ L &= d K(-C_{T_1} - C_{T_2} + C_{T_3} + C_{T_4}) \\ M &= d K(C_{T_1} - C_{T_2} - C_{T_3} + C_{T_4}) \\ N &= \frac{KR}{\sqrt{2}} \left( -|C_{T_1}|^{\frac{3}{2}} + |C_{T_2}|^{\frac{3}{2}} - |C_{T_3}|^{\frac{3}{2}} + |C_{T_4}|^{\frac{3}{2}} \right) \end{aligned} \quad (2.19)$$

For the variable-pitch quadrotor, the control inputs cannot be directly mapped to the actuators as in the case of conventional multirotors. Moreover, the use of virtual control and its nonlinearity in the yaw input has to be taken care of by using dynamic control allocation. This was first proposed in [14]. The basic idea is to use stable first order dynamics to arrive at the desired rate of change of thrust coefficients.

Numerical integration then provides the virtual control inputs ( $C_{T_i}$ 's). The actual blade angles are computed using (2.7).

To ensure simple computation of thrust coefficient derivatives via control input derivatives, stable first-order dynamics are introduced which are given by

$$\dot{T} = k(T_d - T), \quad k > 0. \quad (2.20)$$

This represents stable first order error dynamics for the error  $E = T - T_d$  with  $\dot{T}_d = 0$  which forces  $U_i$  to follow  $T_d$ . Similar first order dynamics can be obtained for the control inputs  $L$ ,  $M$ , and  $N$ . Here, the subscript  $d$  denotes the desired control input that is obtained from the position and attitude control laws. The derivatives of thrust coefficients are computed using the expression

$$\begin{pmatrix} \dot{C}_{T_1} \\ \dot{C}_{T_2} \\ \dot{C}_{T_3} \\ \dot{C}_{T_4} \end{pmatrix} = \begin{pmatrix} \gamma K & \gamma K & \gamma K & \gamma K \\ -\gamma dK & -\gamma dK & \gamma dK & \gamma dK \\ \gamma dK & -\gamma dK & -\gamma dK & \gamma dK \\ -\frac{3KR}{2} \left( \frac{|C_{T_1}|}{2} \right)^{\frac{1}{2}} & \frac{3KR}{2} \left( \frac{|C_{T_2}|}{2} \right)^{\frac{1}{2}} & -\frac{3KR}{2} \left( \frac{|C_{T_3}|}{2} \right)^{\frac{1}{2}} & \frac{3KR}{2} \left( \frac{|C_{T_4}|}{2} \right)^{\frac{1}{2}} \end{pmatrix}^{-1} \begin{pmatrix} \dot{T} \\ \dot{L} \\ \dot{M} \\ \dot{N} \end{pmatrix} \quad (2.21)$$

The blade pitch angles computed from thrust coefficients are converted to pulse-width modulated (PWM) signals for the servos. The servos act as the actuators for changing the collective blade pitch angles.

The gain  $k$  in (2.20) have to be chosen such that the control allocation loop evolves at a rate that is 5-10 times higher than both altitude and attitude closed-loop systems. This means that the steady state values of the collective pitch angles have to be reached well before any change in the desired control input occurs.

# Chapter 3

## Robust Attitude Control Design

Application of PD, PID, and LQ controllers to stabilize quadrotors has been well established [2, 11]. However, a systematic approach to deduce the controller gains such that it satisfies robustness bounds in the presence of parameter uncertainties and model approximations does not exist. In this section, a robust lead compensator design is presented in detail to stabilize roll dynamics of a variable-pitch quadrotor in the presence of parameter uncertainty. A separate section on control synthesis discusses compensator design for both roll and yaw subsystems for conventional quadrotors, conventional hexarotors and variable-pitch quadrotors.

### 3.1 Robust Controller for Roll Dynamics

The nominal model for roll dynamics is given by

$$G_0(s) = \frac{1}{I_{xx} s^2}. \quad (3.1)$$

The set of plants with inverse multiplicative uncertainty can be represented as [19]

$$G(s) = (1 + r \Delta(s))^{-1} G_0(s), \quad (3.2)$$

where  $r = \frac{I_{xx}^{max} - I_{xx}^{min}}{I_{xx}^{max} + I_{xx}^{min}}$  and perturbations  $\Delta(s)$  are assumed to be real which satisfy the condition  $|\Delta(j\omega)| \leq 1, \forall \omega$ . This is illustrated in Fig. 3.1. The terms  $I_{xx}^{max}$  and

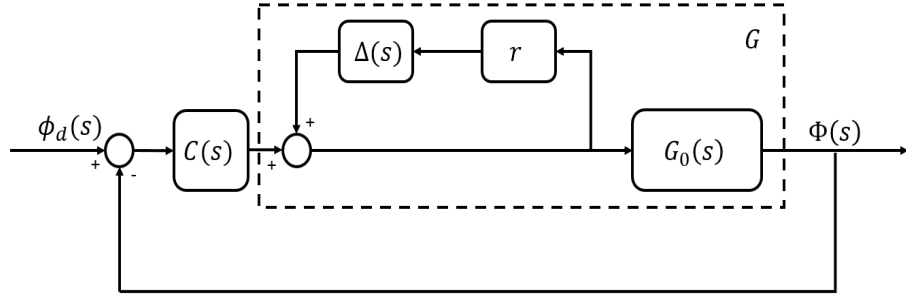


FIGURE 3.1: Roll dynamics with inverse multiplicative uncertainty.

$I_{xx}^{min}$  are defined as

$$I_{xx}^{max} = I_{xx} + \gamma I_{xx}; \quad I_{xx}^{min} = I_{xx} - \gamma I_{xx}, \quad (3.3)$$

where  $0 \leq \gamma < 1$ . Hence, this implies that the controller should be robust to almost 100% variation in parameter estimates. The PD controller in time domain is given by

$$L = K_p(\phi_d - \phi) + K_d \frac{d}{dt}(\phi_d - \phi), \quad (3.4)$$

where  $\phi_d$  is the desired roll angle,  $K_p$ ,  $K_d$  are positive controller gains, and  $L$  is the moment input for roll subsystem. From (3.2) and (3.4), we get

$$GC(s) = (1 + r\Delta)^{-1} \frac{K_d s + K_p}{I_{xx} s^2}. \quad (3.5)$$

However, the PD controller given in (3.4) cannot be implemented in real time as this is a non-causal system. This is also seen by its Laplace transform. A low-pass filter is thus added such that the resulting lead compensator-type transfer function has maximum PM and rejects high frequency oscillations. The modified controller  $C(s)$  is given by

$$C(s) = \frac{K_p(0.25s + 1)}{\tau_d s + 1}. \quad (3.6)$$

We know that a high value of  $K_d$  increases the bandwidth of the system but induces unstable oscillations at the same time. Moreover, it is known that angular velocity evolves 5-10 times faster than the attitude states. Thus, the value of  $K_d$  is chosen such that  $K_d \approx \frac{K_p}{5}$ .

Placing the pole of the lead compensator one decade to the right of the zero is

common practice in loop-shaping-based design to obtain a good amount of PM. Choosing  $\tau_d$  in (3.6) using this rule-of-thumb results in a controller with decent amount of phase margin ( $\approx 55^\circ$ ) for the system given in Table 3.3. The resulting controller is given by

$$C(s) = \frac{K_p(0.25s + 1)}{0.025s + 1}. \quad (3.7)$$

and the resulting Bode plot with  $K_p = 0.35$  is given in Fig. 3.2.

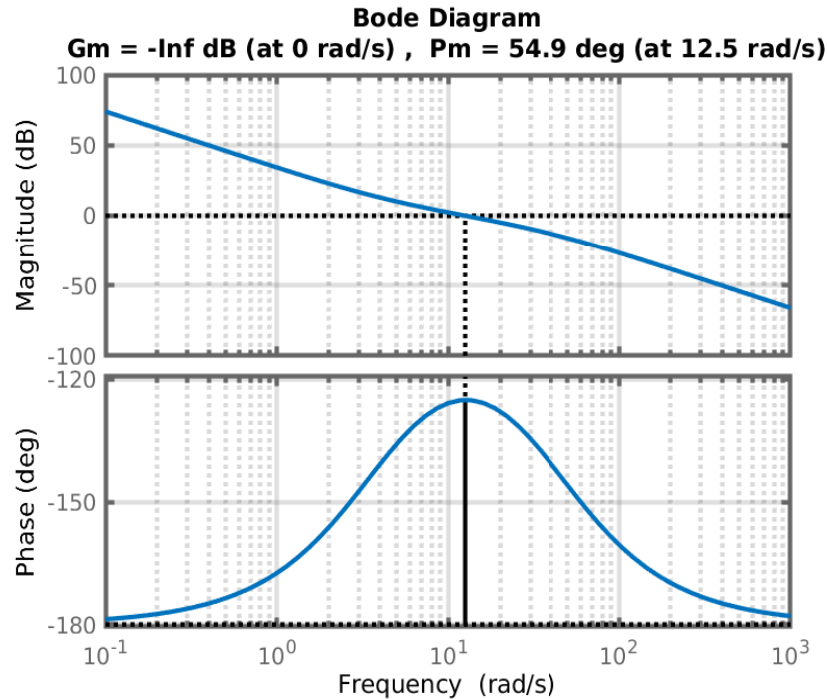


FIGURE 3.2: Bode diagram for  $G_0C(s)$  with the initial control design in (3.7) with  $K_p = 0.35$

However, the value of  $\tau_d$  can be reduced further to achieve higher PM and lower settling times without allowing high frequency noise to degrade controller performance. Knowing the frequency at which the controlled states are estimated plays an important role in deciding the final value of  $\tau_d$ . This is because the value of  $\tau_d$  should only be reduced in a way that it sufficiently attenuates high frequency noise coming in through estimation. In other words, the asymptote with  $-40$  dB/decade slope towards the higher frequency region in Fig. 3.2 should start well before the frequency at which states are being estimated. Since the state estimation frequency is known to be 250 Hz for the autopilot used in this work,  $\tau_d$  is chosen to be 0.002.

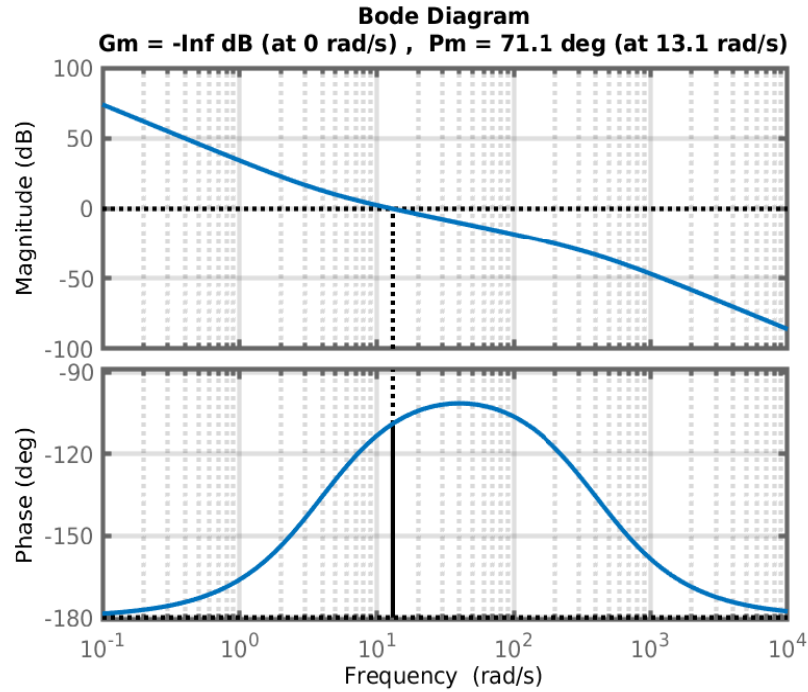


FIGURE 3.3: Bode diagram for  $G_0C(s)$  with the modified control design in (3.8)  
with  $K_p = 0.35$

Now the open loop transfer function  $G_0C(s)$  is fixed, except for the gain  $K_p$ . The new  $C(s)$  is given by

$$C(s) = \frac{K_p(0.25s + 1)}{0.002s + 1}. \quad (3.8)$$

For the example considered in Fig. 3.2, the modified Bode plot is shown in Fig. 3.3. Increasing the value of  $K_p$  to further increase the PM in Fig. 3.3 induces instability to the closed-loop system due to high PD gains. Note that a PM of  $71.1^\circ$  is already high and close to its maximum value ( $\approx 78.6^\circ$ ). This large amount of PM ensures very good tracking and low overshoot. In the coming sections, robust stability analysis of the developed controller and control synthesis for different multirotors are presented. This shows that the proposed compensator can be synthesized quickly with minimal gain tuning and is robust to parameter uncertainties.

### 3.1.1 Robust Stability Analysis

**Lemma 3.1.** *For an open loop gain with inverse multiplicative uncertainty given by*

$$GC(s) = (1 + r \Delta(s))^{-1} G_0 C(s),$$

*the robust stability criterion is given by*

$$|r S(j\omega)| < 1, \quad \forall \omega,$$

*where  $|\Delta(j\omega)| \leq 1, \forall \omega$ , and  $S(j\omega) = \frac{1}{1+G_0C(j\omega)}$  is the sensitivity function.*

*Proof.* The proof is similar to the generalized uncertainty case discussed in Chapter 7 of [19]. Assume that the nominal open loop system  $G_0 C(s)$  is stable. Robust stability is ensured if  $GC(j\omega)$  does not encircle the  $-1+j0$  point. This can be represented using norms as

$$\begin{aligned} & |1 + GC(j\omega)| > 0, \quad \forall GC(j\omega), \quad \forall \omega \\ \Rightarrow & |1 + (1 + r \Delta(j\omega))^{-1} G_0 C(j\omega)| > 0, \quad \forall |\Delta(j\omega)| \leq 1, \quad \forall \omega \\ \Rightarrow & |1 + r \Delta(j\omega) + G_0 C(j\omega)| > 0, \quad \forall |\Delta(j\omega)| \leq 1, \quad \forall \omega. \end{aligned} \quad (3.9)$$

For the worst case in  $|\Delta(j\omega)|$  where  $|\Delta(j\omega)|=1$  and when  $|1 + G_0 C(j\omega)|$  and  $r$  are treated as vectors with an angle of  $180^\circ$  between them, the condition in (3.9) reduces to

$$\begin{aligned} & |1 + G_0 C(j\omega)| - |r| > 0, \quad \forall \omega \\ \Rightarrow & |r S(j\omega)| < 1, \quad \forall \omega. \end{aligned} \quad (3.10)$$

□

In the next section, controller synthesis is presented for conventional multirotors as well as a variable-pitch quadrotor.

## 3.2 Control Synthesis

Control synthesis for a conventional quadrotor in X-configuration, a conventional hexarotor in +-configuration, and a variable-pitch quadrotor is presented in this section. Parameters of the aforementioned vehicles which are used for both simulations and experimental validation are given in Tables 3.1 - 3.3.

### 3.2.1 Conventional Quadrotor

From Table 3.1, we observe that the rotational inertia about the body-fixed  $x_b$ - and  $y_b$ -axes are identical. Hence, control synthesis for only the roll subsystem is presented here. The same controller is used to control the pitch subsystem and is validated using experiments.

Parameter (units)	Value
Mass, $m$	1.8 kg
Radius of rotor blades, $R$	0.15 m
Force coefficient, $k_f$	$2.6193 \times 10^{-5}$ N/(rad/s)
Moment coefficient, $k_m$	$4.4779^{-7}$ N m/(rad/s)
Distance between rotor axis and cg, $d$	0.30 m
Number of blades per rotor, $N_b$	2
Moment of inertia about $x_b$ , $I_{xx}$	0.002 kg m <sup>2</sup>
Moment of inertia about $y_b$ , $I_{yy}$	0.002 kg m <sup>2</sup>
Moment of inertia about $z_b$ , $I_{zz}$	0.005 kg m <sup>2</sup>

TABLE 3.1: Parameters for the conventional quadrotor.

First, a simple lead compensator for the roll subsystem is designed with its zero and pole separated by a decade. This is shown in Fig. 3.4. This provides a good PM of 54.4° but fails to meet the robust stability criterion in (3.10) for  $r = 0.9$  with  $K_p = 0.2$ . This is shown in Fig. 3.5 where satisfying the robust stability criterion becomes difficult with increasing uncertainty while maintaining a decade distance between zero and pole of the compensator.

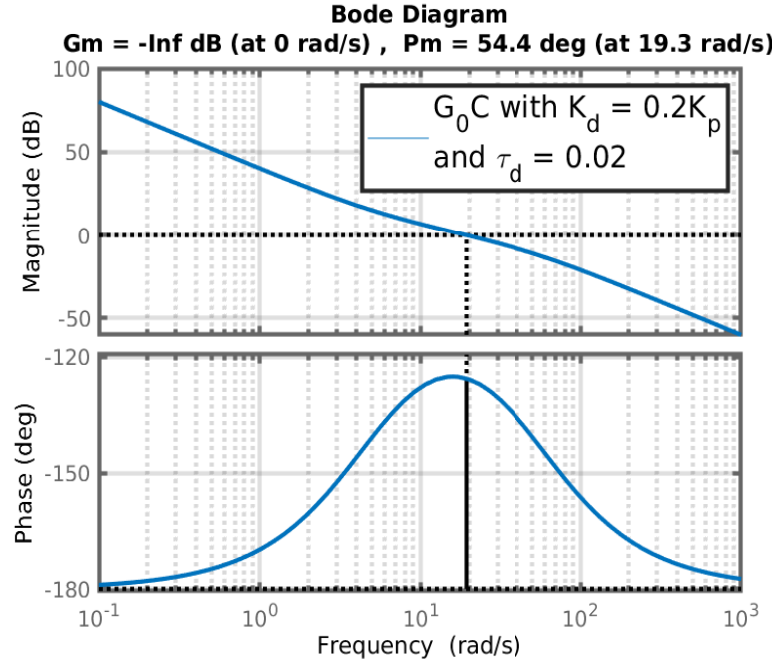


FIGURE 3.4: Bode plot for roll subsystem  $G_0C(s)$  with  $K_p = 0.2$  for the quadrotor parameters given in Table 3.1

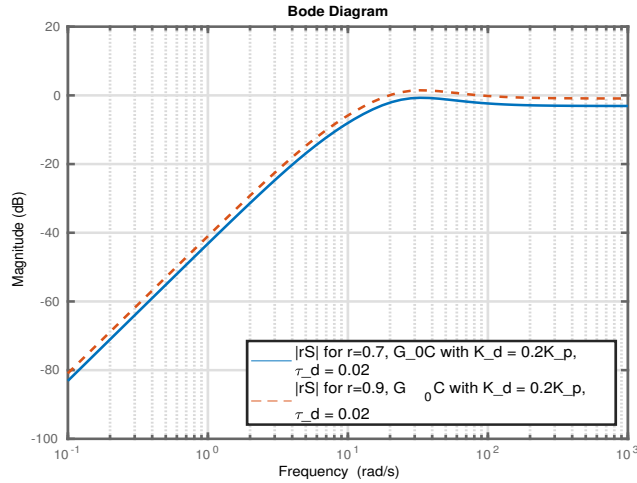


FIGURE 3.5:  $|rS|$  plot for roll subsystem for the quadrotor parameters given in Table 3.1 with  $K_p = 0.2$ . The robust stability criterion is violated when the uncertainty is 90%, which is undesirable.

To achieve better tracking performance with higher PM as well as ensuring that robust stability criterion is satisfied for large uncertainties,  $\tau_d$  is chosen as 0.002. Note that  $\tau_d$  cannot be chosen arbitrarily small. This is to ensure that the effect

of high frequency noise on the controller performance is minimal. The modified compensator design is shown in Fig. 3.6 and robust stability criterion for both 70% and 90% uncertainty is verified in Fig. 3.7.

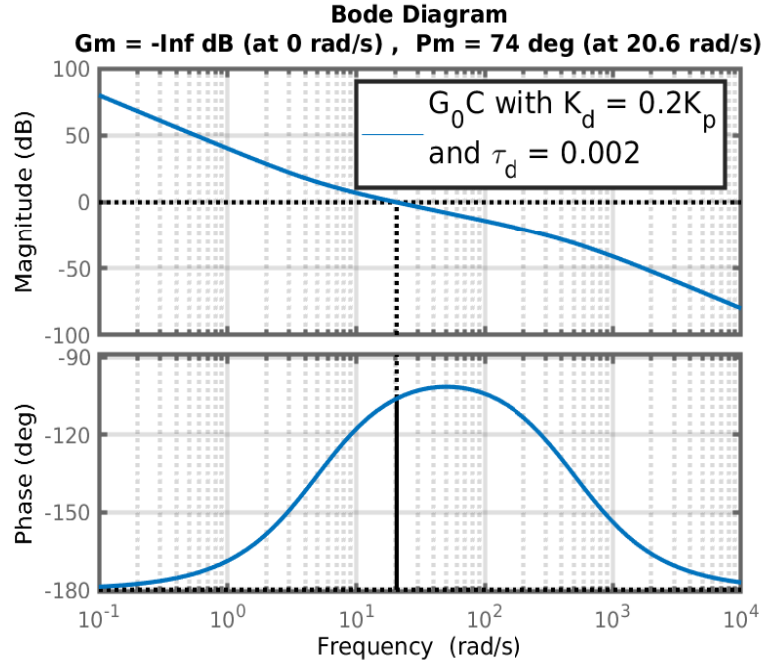


FIGURE 3.6: Modified bode plot for roll subsystem  $G_0C(s)$  for the quadrotor parameters given in Table 3.1

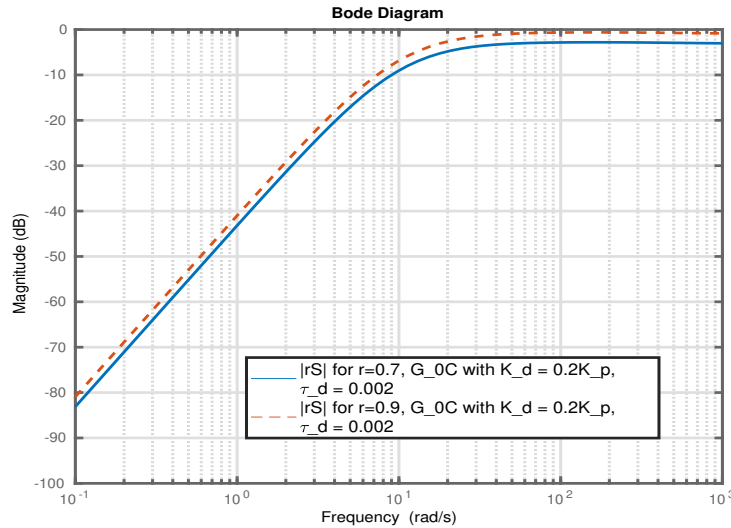


FIGURE 3.7:  $|rS|$  plot for roll subsystem for the quadrotor parameters given in Table 3.1. The robust stability criterion is satisfied for both cases of uncertainty.

Control synthesis for the yaw subsystem is presented next for the conventional quadrotor considered in Table 3.1. The open loop Bode plot for  $G_0C$  is shown in Fig. 3.8 for both values of  $\tau_d$ . Here,  $G_0(s) = \frac{1}{I_{zz}s^2}$ .

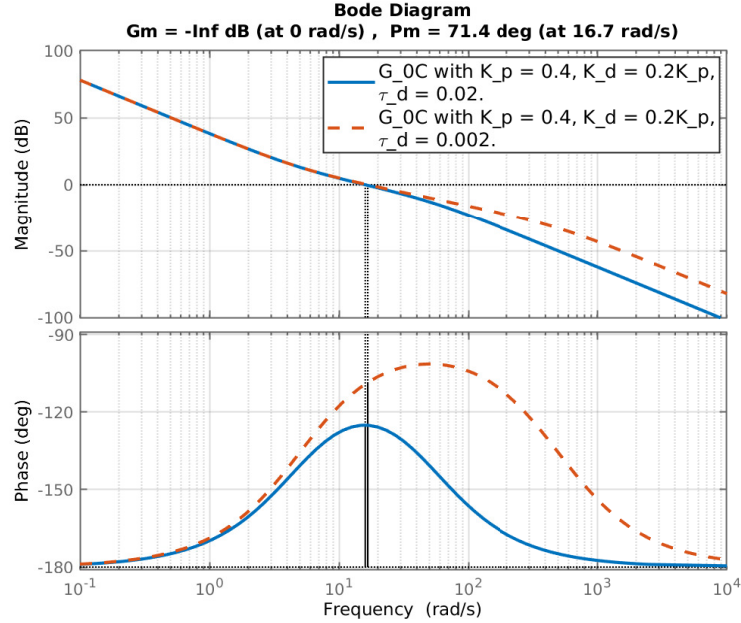


FIGURE 3.8: Bode plot for yaw subsystem for the quadrotor parameters given in Table 3.1

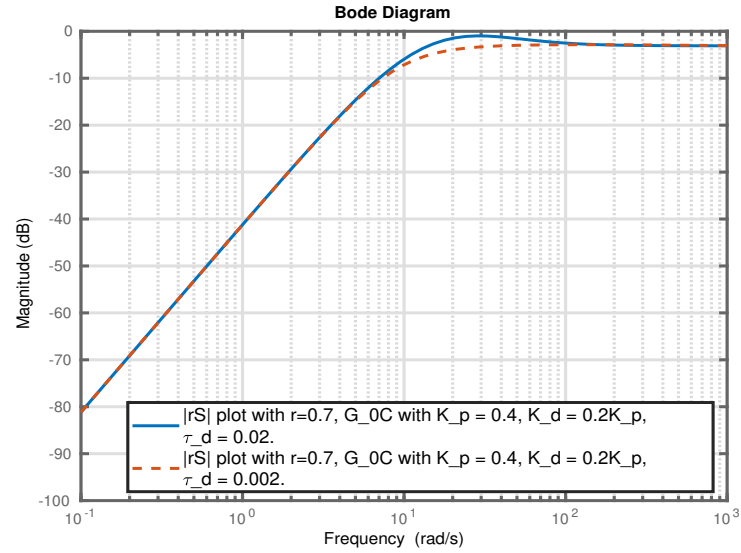


FIGURE 3.9:  $|rS|$  plot for yaw subsystem for the quadrotor parameters given in Table 3.1. Robust stability criterion is satisfied for  $r = 0.7$  for both values of  $\tau_d$ .

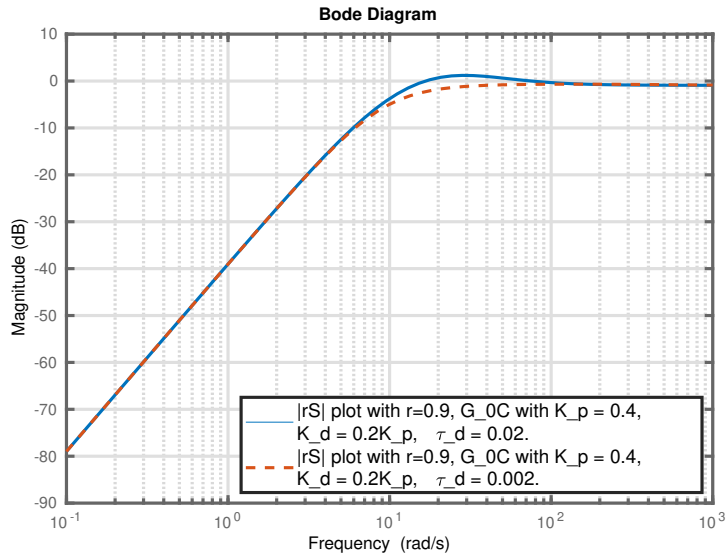


FIGURE 3.10:  $|rS|$  plot for yaw subsystem for the quadrotor parameters given in Table 3.1. Robust stability criterion is satisfied for  $r = 0.9$  and  $\tau_d = 0.002$  whereas it fails for  $r = 0.9$  and  $\tau_d = 0.02$ .

Robust stability criterion is verified for the yaw subsystem in Fig. 3.9 and 3.10 for different uncertainties. It can be observed that choosing a smaller  $\tau_d$  is beneficial for ensuring robustness to high levels of parametric uncertainty.

### 3.2.2 Conventional Hexarotor

Parameter (units)	Value
Mass, $m$	2.0 kg
Radius of rotor blades, $R$	0.127 m
Force coefficient, $k_f$	$1.3934 \times 10^{-5}$ N/(rad/s)
Moment coefficient, $k_m$	$2.1965^{-7}$ N m/(rad/s)
Distance between rotor axis and cg, $d$	0.28 m
Number of blades per rotor, $N_b$	2
Moment of inertia about $x_b$ , $I_{xx}$	0.003 kg m <sup>2</sup>
Moment of inertia about $y_b$ , $I_{yy}$	0.003 kg m <sup>2</sup>
Moment of inertia about $z_b$ , $I_{zz}$	0.006 kg m <sup>2</sup>

TABLE 3.2: Parameters for the conventional hexarotor.

Control synthesis for a conventional hexarotor is presented in this section. The parameters for this vehicle are given in Table 3.2. The steps followed for control synthesis for roll and yaw subsystems are similar to those for the conventional quadrotor. The bode plot for the roll subsystem with  $K_p = 0.25$  is shown in Fig. 3.11. A phase margin of  $54.9^\circ$  is obtained with  $\tau_d = 0.02$  and a PM of  $71.4^\circ$  is achieved with  $\tau_d = 0.002$ . Robust stability criterion is verified for different values of  $\tau_d$  as well as  $r$  for the roll subsystem in Fig. 3.12.

The bode plot for the yaw subsystem ( $G_0 = \frac{1}{I_{zz}s^2}$ ) is shown in Fig. 3.13 with  $K_p = 0.45$  and for two different values of  $\tau_d$ . A phase margin of  $54.9^\circ$  is obtained with  $\tau_d = 0.02$  and a PM of  $70.6^\circ$  is achieved with  $\tau_d = 0.002$ . Robust stability criterion is verified through Fig. 3.14 for the yaw subsystem of the hexarotor.

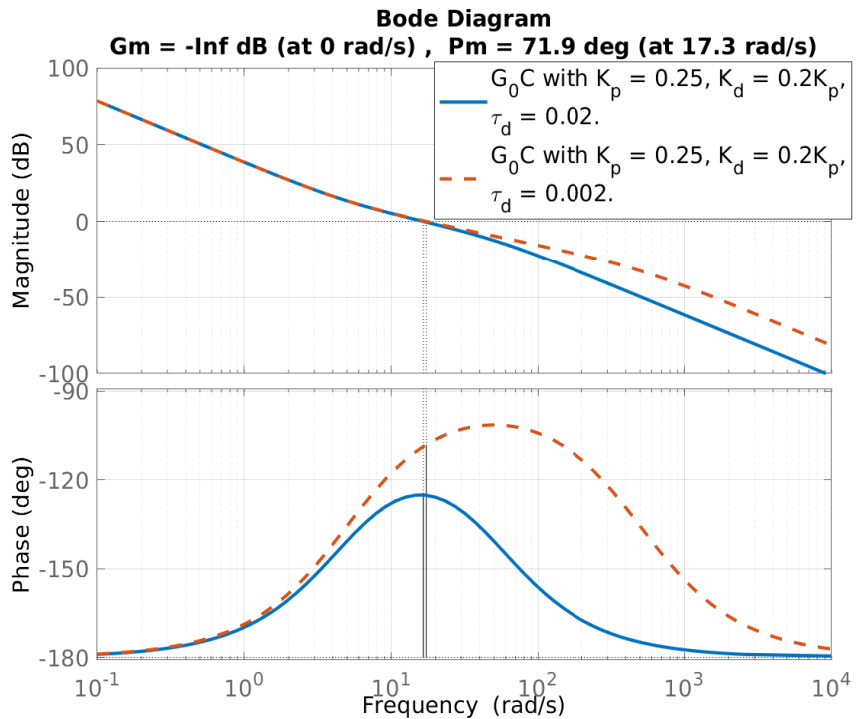


FIGURE 3.11: Bode plot based design for roll subsystem for the hexarotor parameters given in Table 3.2

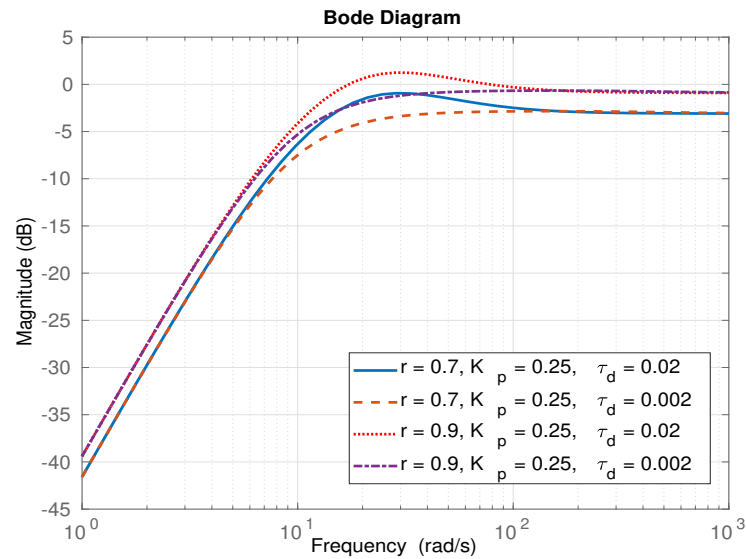


FIGURE 3.12:  $|rS|$  plot for roll subsystem for the hexarotor parameters given in Table 3.2.

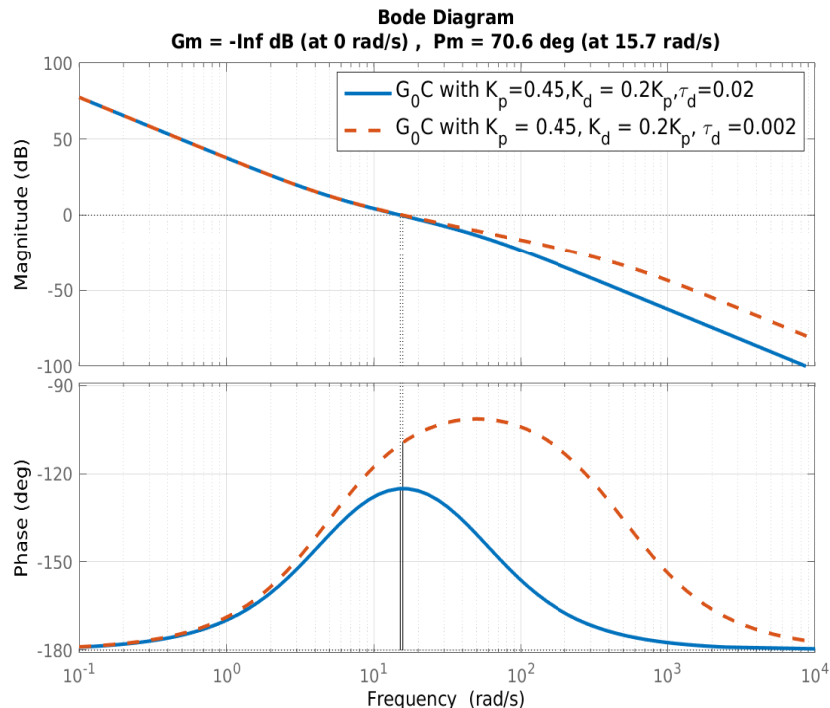


FIGURE 3.13: Bode plot based design for yaw subsystem for the hexarotor parameters given in Table 3.2

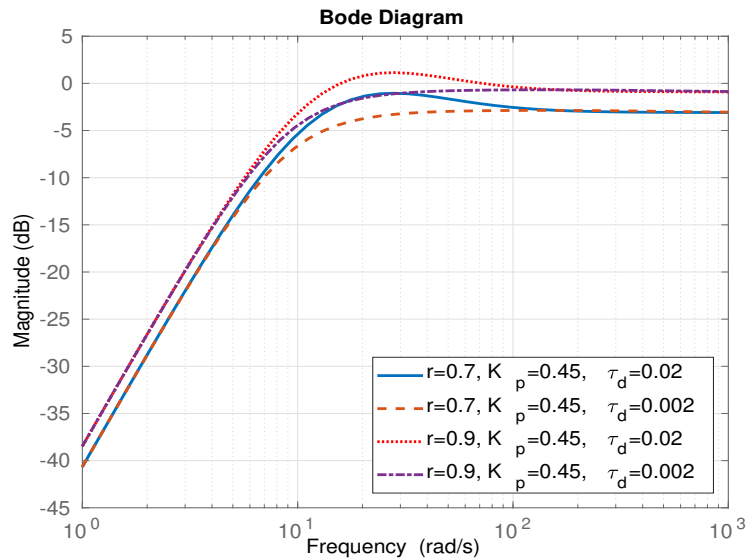


FIGURE 3.14:  $|rS|$  plot for yaw subsystem for the hexarotor parameters given in Table 3.2.

### 3.2.3 Variable-pitch Quadrotor

Parameter (units)	Value
Mass, $m$	1.2 kg
Radius of rotor blades, $R$	0.145 m
Chord length of blades, $c$	0.030 m
Distance between rotor axis and cg, $d$	0.3 m
Slope of airfoil lift curve, $C_{l\alpha}$	5.73 rad <sup>-1</sup>
Number of blades per rotor, $N_b$	2
Rotational speed, $\Omega$	3000 rpm
Moment of inertia about $x_b$ , $I_{xx}$	0.007 kg m <sup>2</sup>
Moment of inertia about $y_b$ , $I_{yy}$	0.007 kg m <sup>2</sup>
Moment of inertia about $z_b$ , $I_{zz}$	0.033 kg m <sup>2</sup>

TABLE 3.3: Parameters for the variable-pitch quadrotor.

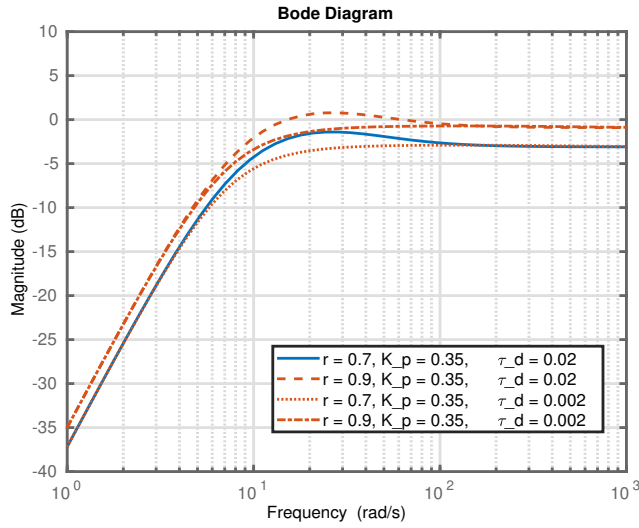


FIGURE 3.15:  $|rS|$  plot for roll subsystem for the quadrotor parameters given in Table 3.3.

Compensator synthesis for the variable-pitch quadrotor with parameters in Table 3.3 was discussed in previous sections using Fig. 3.2 and 3.3. This compensator is used to control the roll and pitch subsystems and is validated experimentally. Robust stability criterion is verified for different values of  $\tau_d$  and  $r$ . This is shown in Fig. 3.15. Next, control synthesis for the yaw subsystem is presented.

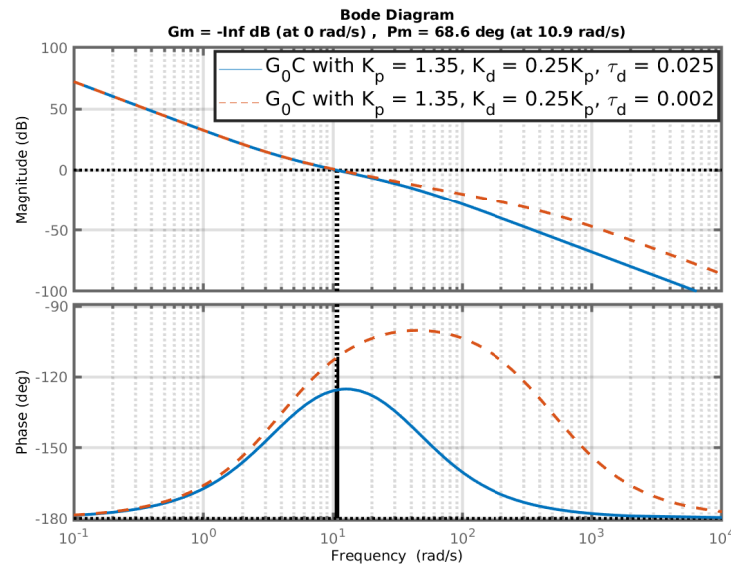


FIGURE 3.16: Bode plot based design for yaw subsystem for the quadrotor parameters given in Table 3.3

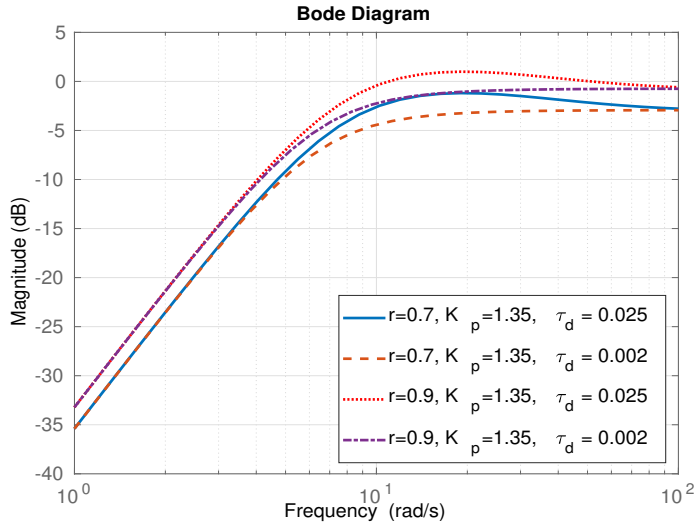


FIGURE 3.17:  $|rS|$  plot for yaw subsystem for the quadrotor parameters given in Table 3.3.

From Fig. 3.16 and 3.17, we obtain the compensator for the yaw subsystem ( $G_0 = \frac{1}{I_{zz}s^2}$ ) of the variable-pitch quadrotor with parameters given in Table 3.3. Simulation and experimental validation of the proposed compensator design is presented in the next chapter.

# Chapter 4

## Results

This chapter presents numerical simulations and experiments for a conventional quadrotor in X-configuration, a conventional hexarotor in +-configuration, and a variable-pitch quadrotor. This validates the proposed methodology and shows robustness to parameter changes.

### 4.1 Simulation Results

In this section, numerical simulations to demonstrate the tracking performance of the designed compensator is presented. The simulation environment utilized for this purpose is MATLAB. The 6-DoF model is numerically simulated using the Runge-Kutta method. Outputs of the roll, pitch, and yaw subsystem compensators are used to generate the appropriate actuator signals (rotor speeds for conventional multirotors and blade-pitch angles for variable-pitch quadrotor). Control inputs generated through (2.10), (2.17), and (2.19) are finally fed to the 6-DoF rigid-body dynamics simulation to obtain the desired tracking response for a conventional quadrotor, a conventional hexarotor, and a variable-pitch quadrotor, respectively.

### 4.1.1 Conventional Quadrotor

Roll tracking response is shown for a conventional quadrotor with parameters given in Table 3.1. The reference signal is a sinusoid with an amplitude of  $20^\circ$ . The frequency of the sinusoid is varied near the cross over frequency of the bode magnitude plot in Fig. 3.6. The compensator is simulated with  $K_p = 0.2$  and  $\tau_d = 0.002$  which is also implemented on the actual UAV while conducting real-world experiments. The simulation experiments are also carried out by changing the quadrotor parameters to show tracking performance in the absence and presence of parametric uncertainty. The pitch and yaw subsystems are shown to be stabilized at  $0^\circ$  since experiments are able to show their tracking capabilities during actual flight.

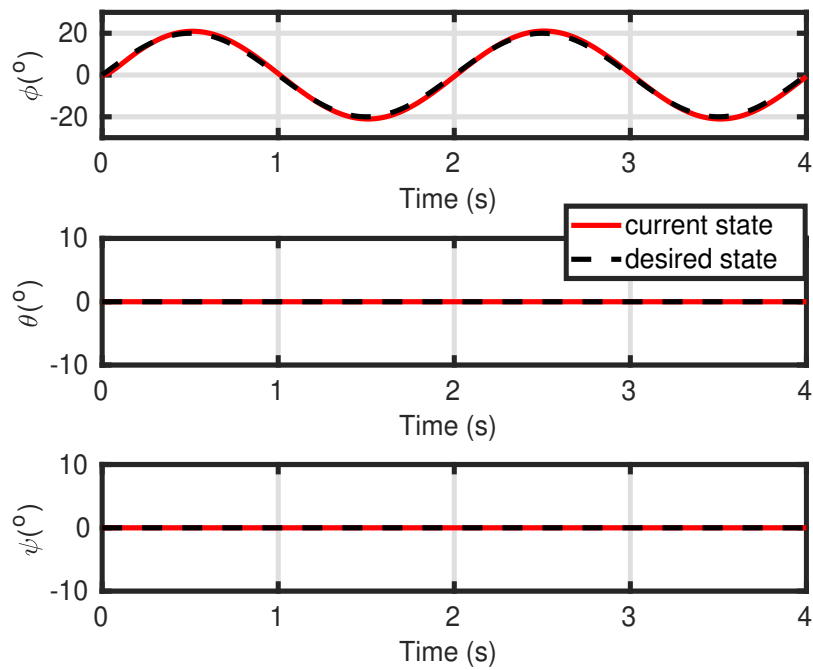


FIGURE 4.1: Roll angle tracking for a sinusoidal reference signal with amplitude  $20^\circ$  and frequency 0.5 Hz. Parameters considered for the rigid-body dynamics simulations are given in Table 3.1.

First, roll tracking is simulated for a reference signal frequency of 0.5 Hz (lesser than the gain crossover frequency) in Fig. 4.1. As expected for no parameter variation, the tracking is very good. The rotor speeds for this simulation experiment are given in Fig. 4.2.

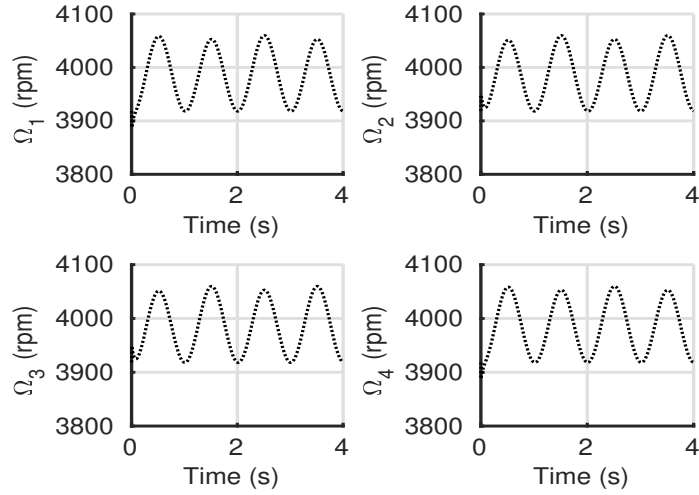


FIGURE 4.2: Rotor speeds obtained using (2.12) for roll tracking in Fig. 4.1.

To show robustness to parameter variation, the same simulation is run with a model that has 70% variation in  $I_{xx}$ ,  $I_{yy}$ , and  $I_{zz}$  ( $r = 0.7$ ).

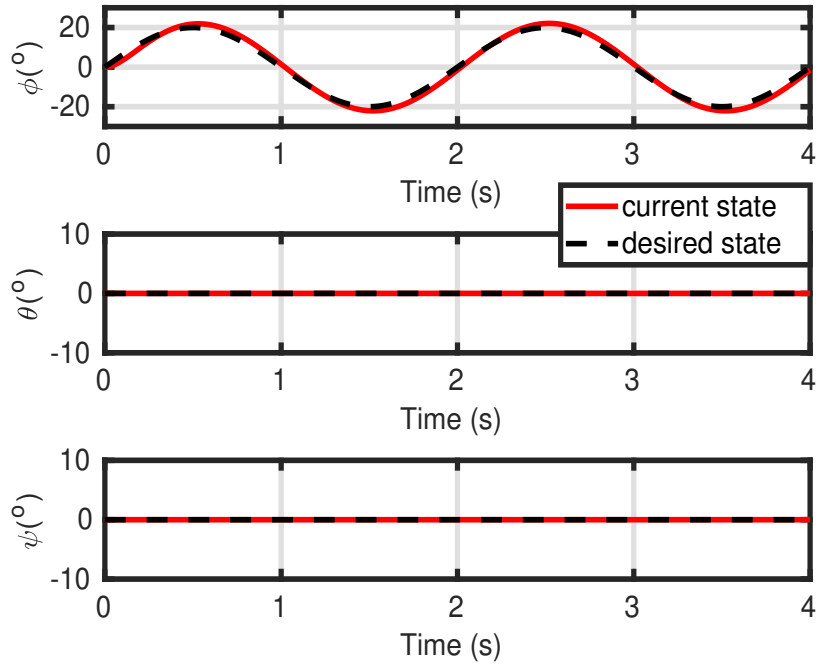


FIGURE 4.3: Roll angle tracking for a sinusoidal reference signal with amplitude 20° and frequency 0.5 Hz. Parameters considered for the rigid-body dynamics simulations are 70% deviated from those given in Table 3.1 which creates an uncertainty of  $r = 0.7$ .

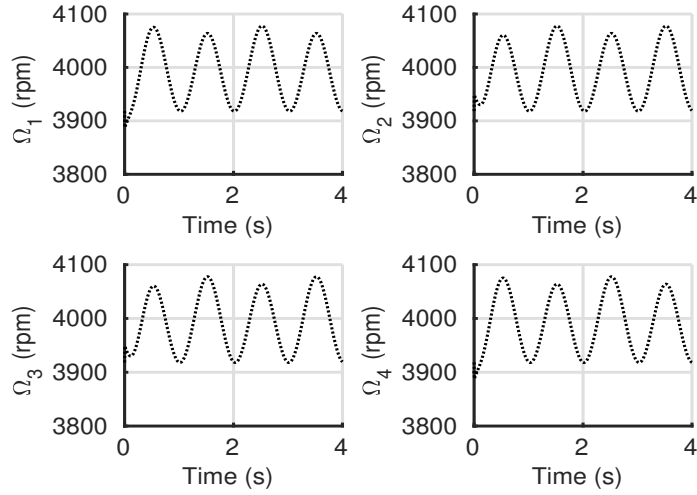


FIGURE 4.4: Rotor speeds obtained using (2.12) for roll tracking in Fig. 4.3.

Since the compensator is robust to parametric uncertainties by design, the tracking performance does not degrade with a 70% change in model parameters. The rotor speeds for this simulation experiment are given in Fig. 4.4. Comparing the tracking responses with and without parametric uncertainties, as shown in Fig. 4.1 and 4.3, respectively, we observe that the vehicle is able to track the reference signal with very little error. It can also be seen that the phase difference between the reference and output sinusoids as well as the error amplitude is minimal. This phase difference and error amplitude keeps increasing with increase in input frequency. This trend is expected from the Bode plots of  $G_0C(s)$  and is also observed by comparing the tracking responses in Fig. 4.1 and 4.5.

Next, tracking a fast changing signal is simulated to show tracking capabilities closer to the gain crossover frequency (3 Hz in this case). A sinusoid of amplitude 20° and frequency 2 Hz is given as the reference signal. Tracking response is shown in Fig. 4.5. It can be observed that tracking is fairly satisfactory and the closed-loop system remains stable. Reference signals that vary faster than 2 Hz are seldom found in real-world flights even during aggressive maneuvers. Hence, the designed compensator can easily be implemented for good tracking performance.

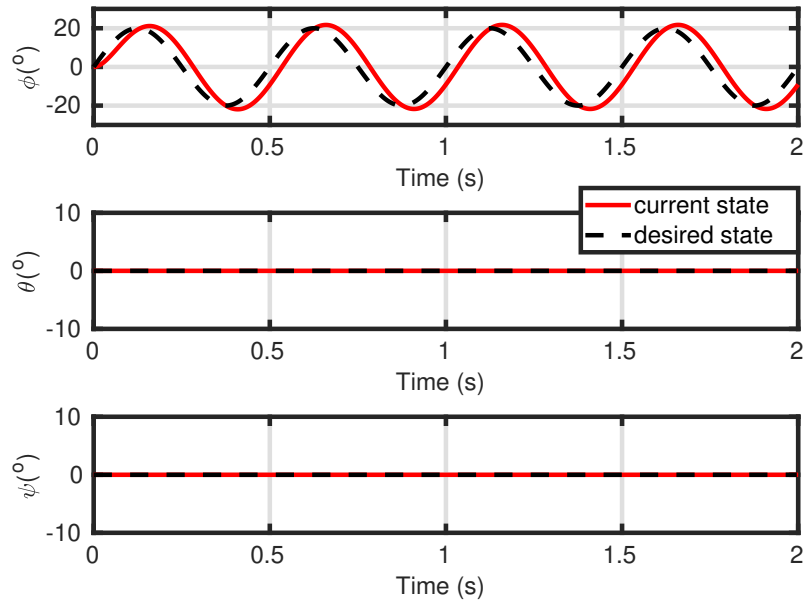


FIGURE 4.5: Roll angle tracking for a sinusoidal reference signal with amplitude  $20^\circ$  and frequency 2 Hz. Parameters considered for the rigid-body dynamics simulations are same as those given in Table 3.1.

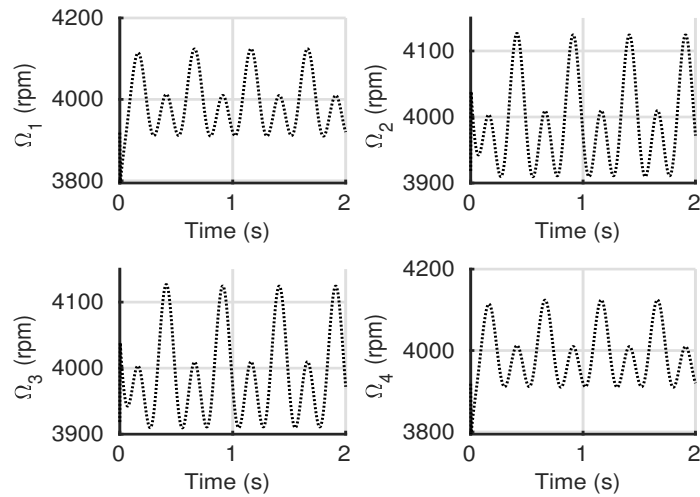


FIGURE 4.6: Rotor speeds obtained using (2.12) for roll tracking in Fig. 4.5.

### 4.1.2 Conventional Hexarotor

Numerical simulations analogous to the conventional quadrotor are carried out in this section for a conventional hexarotor. Parameters for the hexarotor used for simulations are given in Table 3.2. Tracking response of the hexarotor for a reference signal with  $20^\circ$  amplitude and 0.5 Hz frequency is shown in Fig. 4.7 without any uncertainty in the inertia parameters. The corresponding rotor speeds are shown in Fig. 4.8.

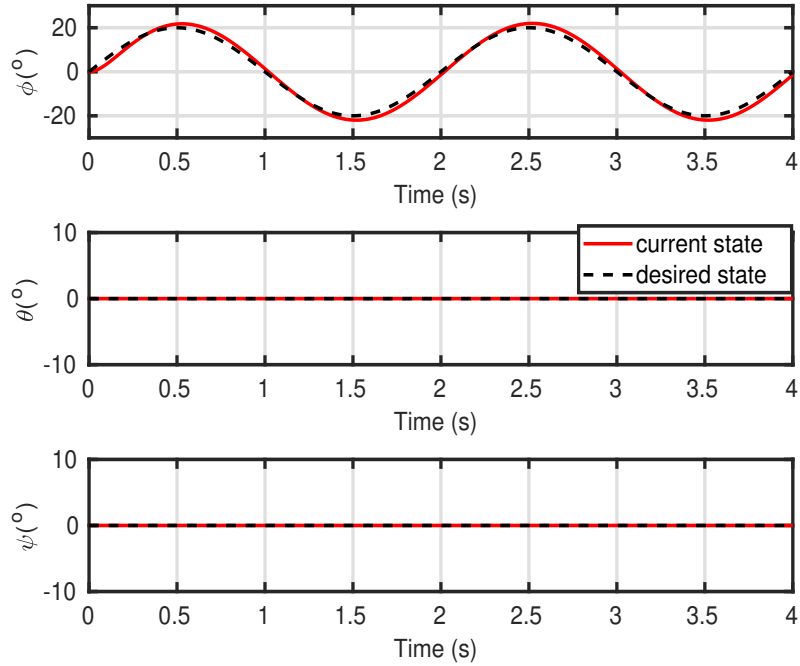


FIGURE 4.7: Roll angle tracking for a sinusoidal reference signal with amplitude  $20^\circ$  and frequency 0.5 Hz. Parameters considered for the rigid-body dynamics simulations are given in Table 3.2.

Next, the same reference signal is used with 70% parameter uncertainty and the tracking response is shown in Fig. 4.9. The corresponding rotor speeds are shown in Fig. 4.10.

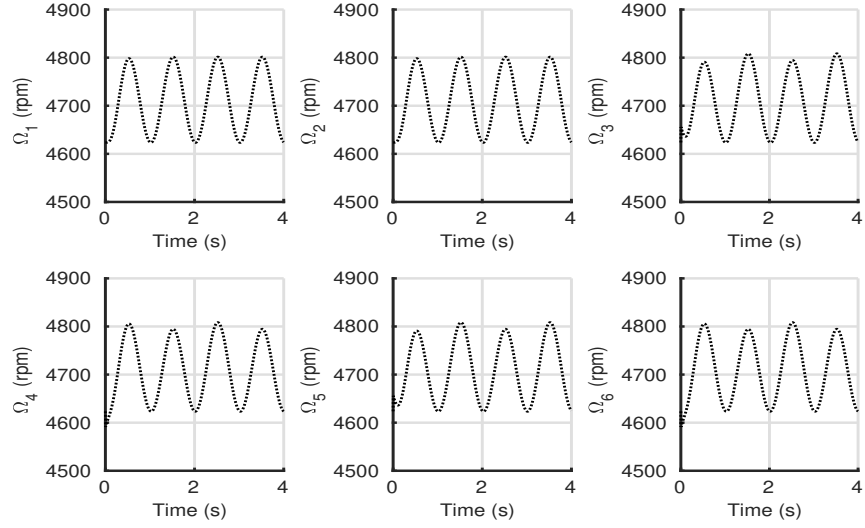


FIGURE 4.8: Rotor speeds obtained using (2.18) for roll tracking in Fig. 4.7.

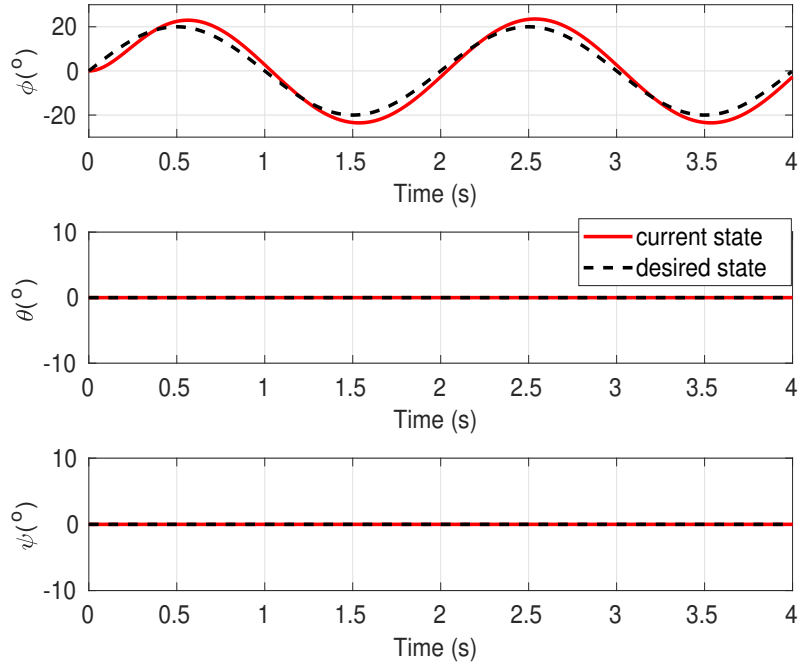


FIGURE 4.9: Roll angle tracking for a sinusoidal reference signal with amplitude  $20^\circ$  and frequency 0.5 Hz. Parameters considered for the rigid-body dynamics simulations are 70% deviated from those given in Table 3.2 which creates an uncertainty of  $r = 0.7$ .

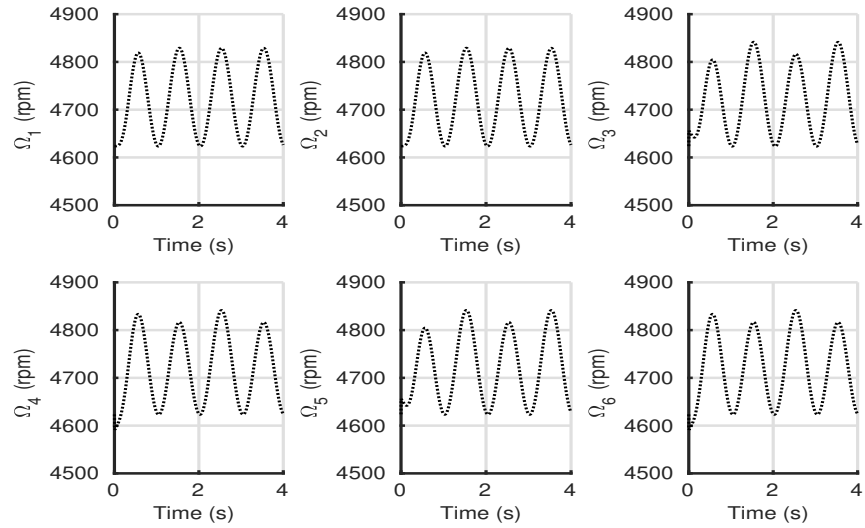


FIGURE 4.10: Rotor speeds obtained using (2.18) for roll tracking in Fig. 4.9.

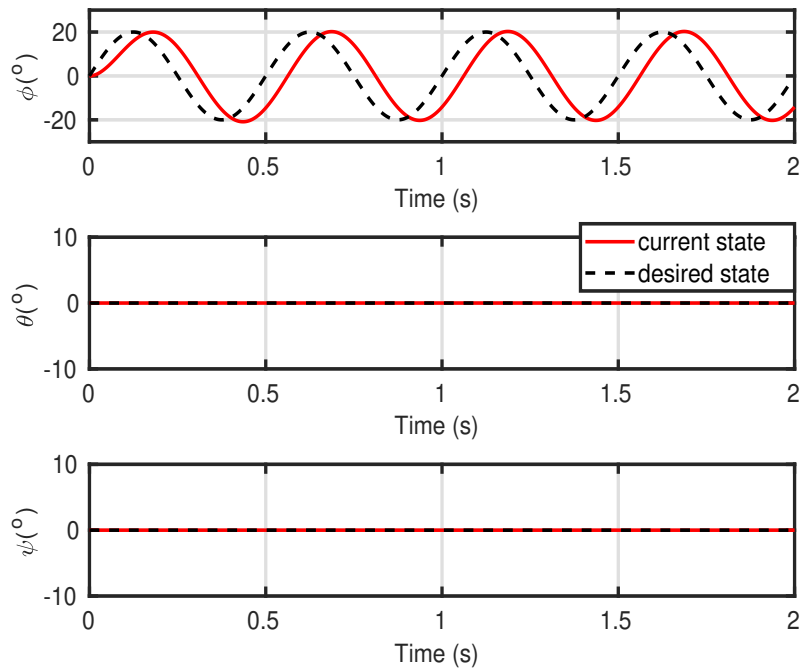


FIGURE 4.11: Roll angle tracking for a sinusoidal reference signal with amplitude  $20^\circ$  and frequency 2 Hz. Parameters considered for the rigid-body dynamics simulations are given in Table 3.2.

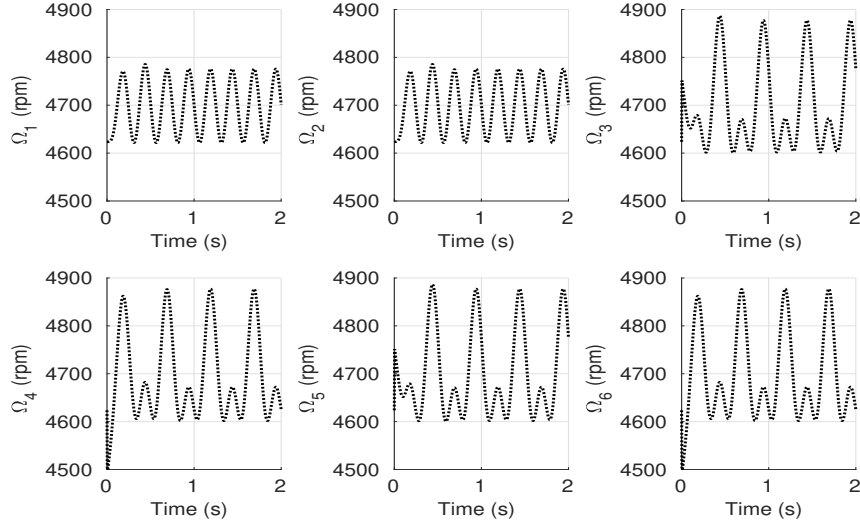


FIGURE 4.12: Rotor speeds obtained using (2.18) for roll tracking in Fig. 4.11.

Tracking response with a sinusoidal reference signal with amplitude  $20^\circ$  and frequency 2 Hz (close to the gain crossover frequency at 2.75 Hz) is shown in Fig. 4.11. Phase difference between reference and output signals is slightly higher than that observed in Fig. 4.6 since the reference signal frequency is closer to the gain crossover frequency for the hexarotor case. The corresponding rotor speeds are shown in Fig. 4.12.

### 4.1.3 Variable-pitch Quadrotor

In this section, numerical simulations are carried out to validate the proposed compensator for the variable-pitch quadrotor with parameters given in Table 3.3. The reference trajectories are identical to those given for the conventional quadrotor in the previous sections.

A comparison of tracking performance with no parameter variation and with 70% parameter variation is shown for the variable-pitch quadrotor first. The tracking responses for the aforementioned cases are shown in Fig. 4.13 and 4.15, respectively. It can be observed that the compensator performs reasonably well in both cases. The thrust coefficients that act as virtual controls and the blade pitch angles which are the final actuators are shown in Fig. 4.14 and 4.16. The values are high since

the vehicle used is off-the-shelf and is ill-designed. Blade pitch angles are close to stall and this should be avoided in future designs of the vehicle.

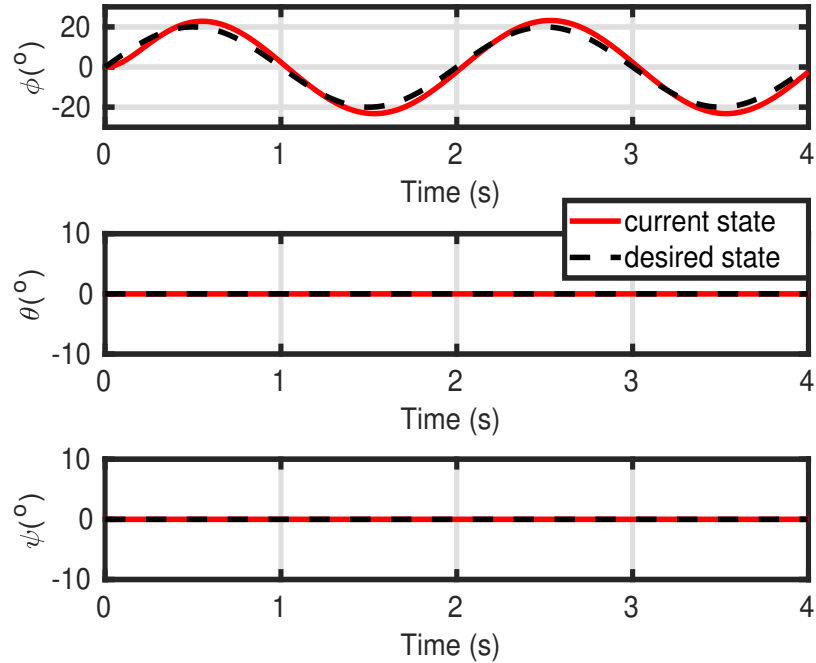


FIGURE 4.13: Roll angle tracking for a sinusoidal reference signal with amplitude  $20^\circ$  and frequency  $0.5$  Hz. Parameters considered for the rigid-body dynamics simulations are identical to those given in Table 3.3.

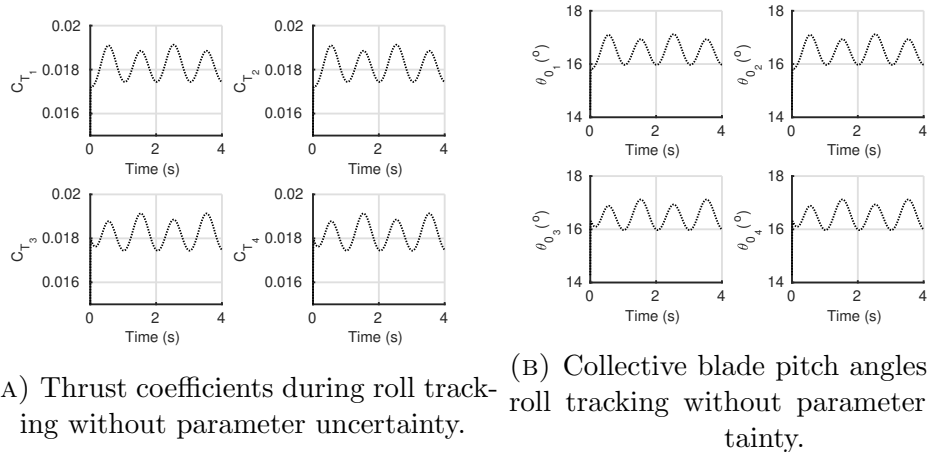


FIGURE 4.14: Thrust coefficients (virtual controls) and collective blade pitch angles (actuators) for roll tracking in Fig. 4.13.

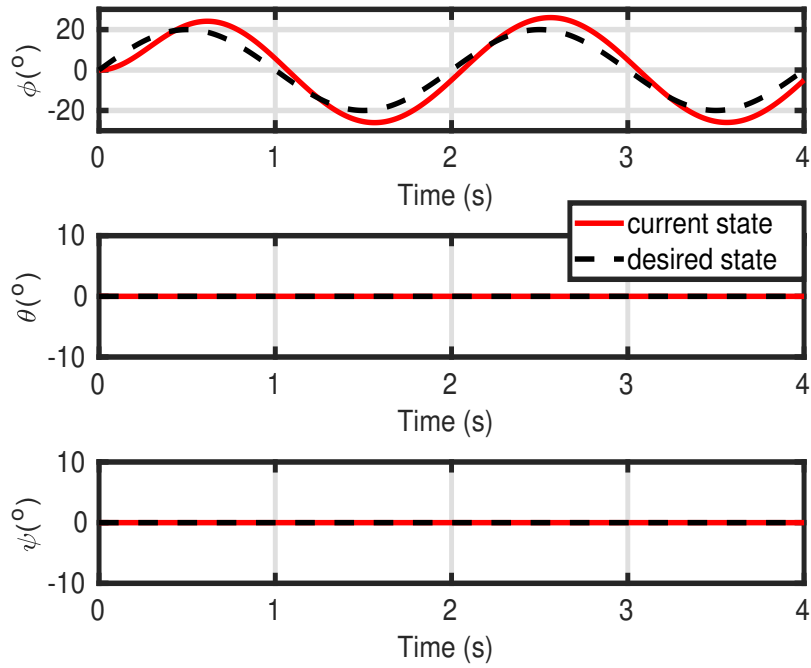
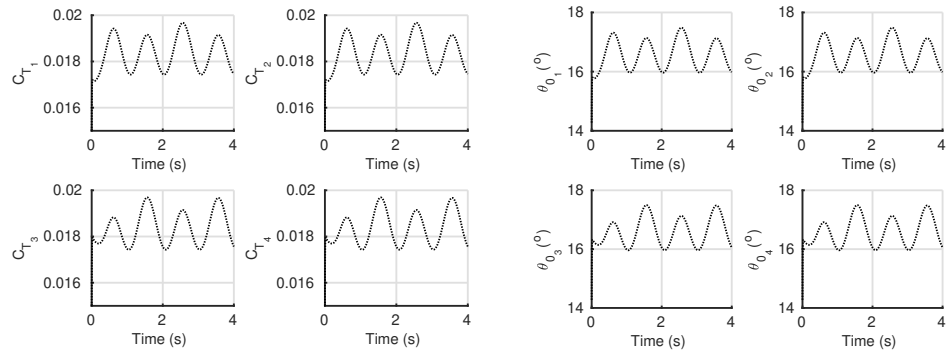


FIGURE 4.15: Roll angle tracking for a sinusoidal reference signal with amplitude 20° and frequency 0.5 Hz. Parameters considered for the rigid-body dynamics simulations are 70% deviated from those given in Table 3.3.



(A) Thrust coefficients during roll tracking with  $r = 0.7$ . (B) Collective blade pitch angles during roll tracking with  $r = 0.7$ .

FIGURE 4.16: Thrust coefficients (virtual controls) and collective blade pitch angles (actuators) for roll tracking in Fig. 4.15.

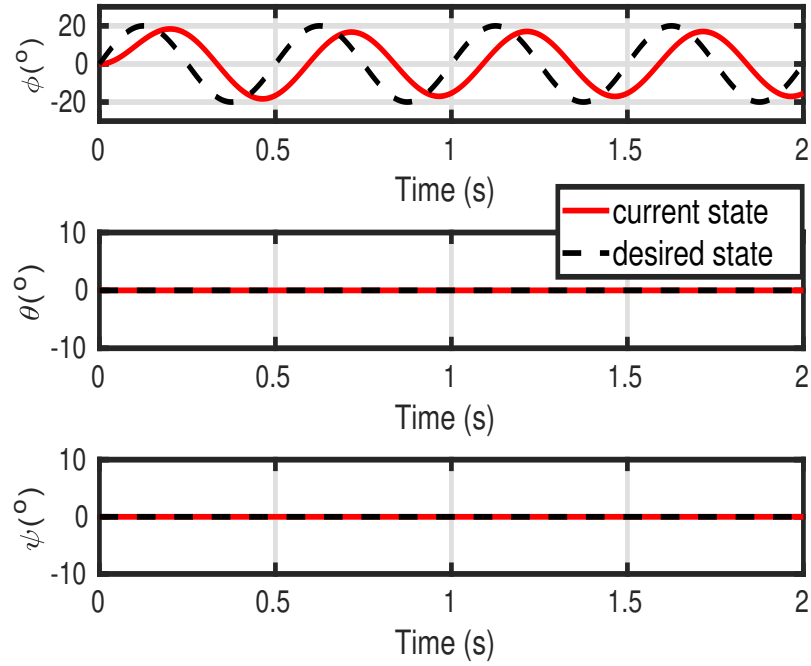
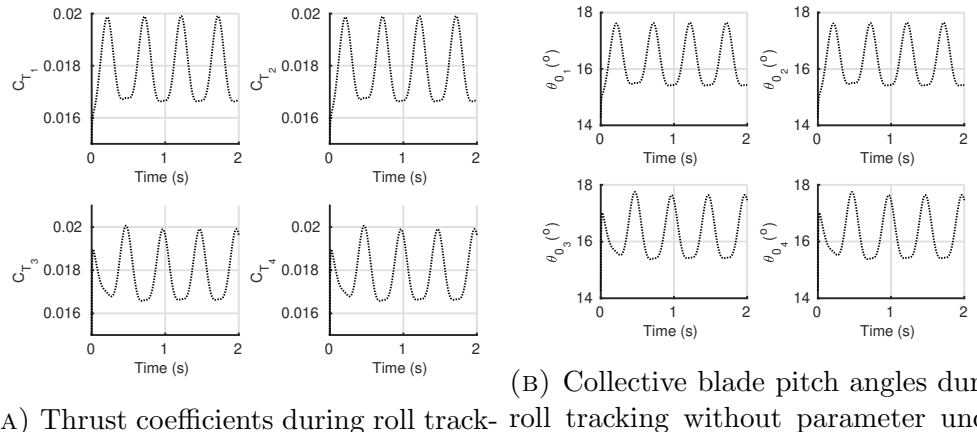


FIGURE 4.17: Roll angle tracking for a sinusoidal reference signal with amplitude  $20^\circ$  and frequency  $0.5$  Hz. Parameters considered for the rigid-body dynamics simulations are identical to those given in Table 3.3.



(A) Thrust coefficients during roll track-

roll tracking without parameter uncer-

tainty.

(B) Collective blade pitch angles during

roll tracking without parameter uncer-

tainty.

FIGURE 4.18: Thrust coefficients (virtual controls) and collective blade pitch angles (actuators) for roll tracking in Fig. 4.17.

Next, the tracking response of the closed-loop system is shown for a reference signal of amplitude  $20^\circ$  and  $2$  Hz in Fig. 4.17. Tracking performance of the compensator

is degraded as compared to the conventional quadrotor and conventional hexarotor since the reference signal frequency is exactly equal to the gain crossover frequency of  $G_0C(s)$  for the variable-pitch quadrotor case. The associated thrust coefficients and blade pitch angles are shown in Fig. 4.18.

In the next section, experimental results of the proposed roll, pitch, and yaw compensators are shown. This validates the proposed method and its robustness to uncertain parameter estimates.

## 4.2 Experimental Results

In order to validate the proposed compensator on actual UAVs, an open source flight controller is used in this work. Pixhawk autopilot developed by 3D Robotics is a widely used platform to validate and test UAV control and estimation algorithms. The autopilot is fixed rigidly onto the multirotor UAVs as shown in Fig. 1.2 and 1.3.

The flight stack (software stack) used is PX4 [20]. The flight stack is open source software used by developers to ensure stability of an UAV at the lowest level. The flight stack is unix-like and runs a real-time operating system (RTOS). It uses a publish-subscribe architecture which makes it easy to use and modular in nature. The PX4 flight stack by default carries several modules for control, estimation, navigation, etc. A separate module for the attitude controller is created and built to validate the compensators proposed in this work. An EKF running onboard the autopilot provides fairly accurate estimates of the roll, pitch, and yaw angles along with the body angular rates. Flight results for both the conventional and variable-pitch quadrotors along with a conventional hexarotor are given in the following sections.

### 4.2.1 Conventional Quadrotor



FIGURE 4.19: Conventional quadrotor in hover condition.

The lead compensator in (3.8) is implemented on the conventional quadrotor with  $K_p$  identical to that used in the simulations. The tracking response is shown in Fig. 4.20. The reference inputs were given manually through a radio controller which simplified the testing process. The tracking response is fairly good for both fast and slow changing reference signals and is able to hover in a stable manner. A screen grab of the video shows the quadrotor in hover (see Fig. 4.19) and during various maneuvers (see Fig. 4.21 and 4.22).

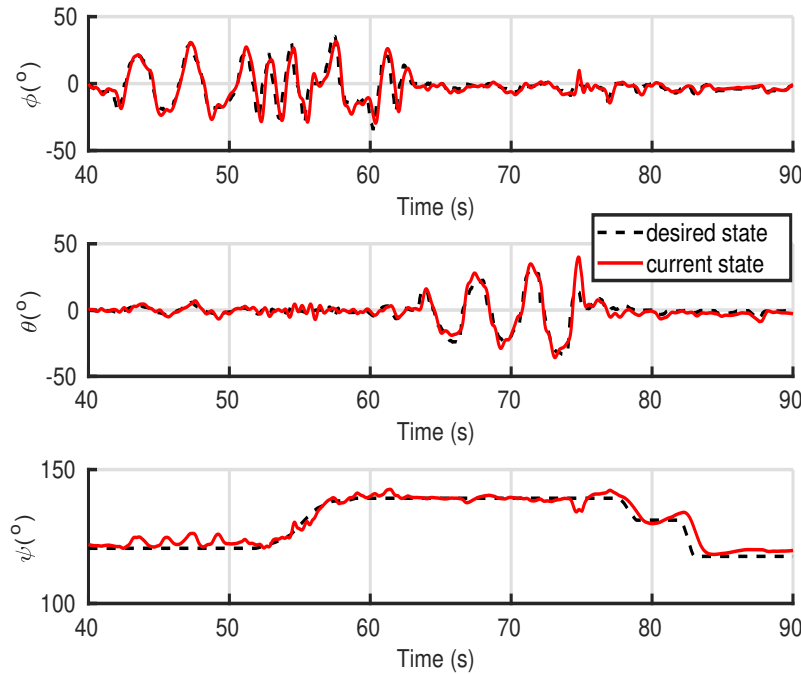
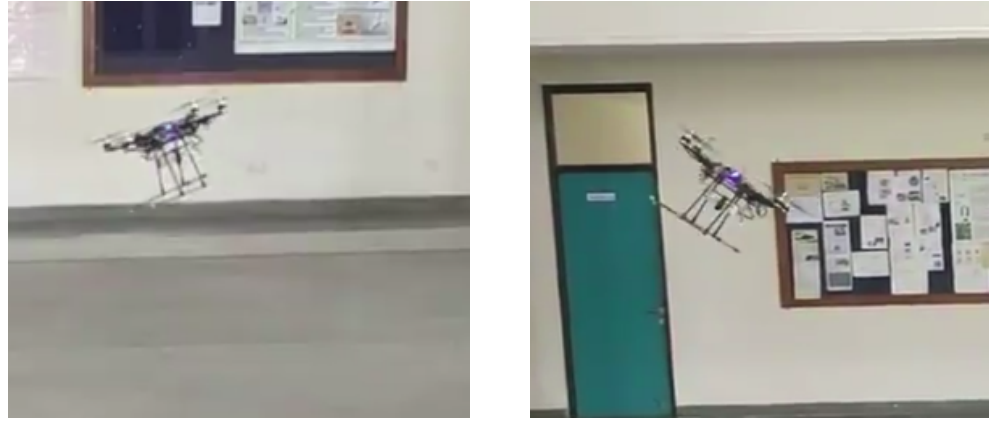


FIGURE 4.20: Roll, pitch, and yaw tracking using the conventional quadrotor in Fig. 1.2 (A). The compensator synthesized in Fig. 3.6 is used for the roll and pitch tracking for this vehicle. The compensator synthesized in Fig. 3.8 is used for yaw subsystem control.



(A) Quadrotor on the ground. (B) Quadrotor with a negative roll angle.

FIGURE 4.21: Screen grabs of the conventional quadrotor during test flights.



(A) Quadrotor with negative pitch angle (pitch down motion). (B) Quadrotor with positive pitch angle (pitch up motion).

FIGURE 4.22: Screen grabs of the conventional quadrotor performing pitch up and down maneuvers.

#### 4.2.2 Conventional Hexarotor

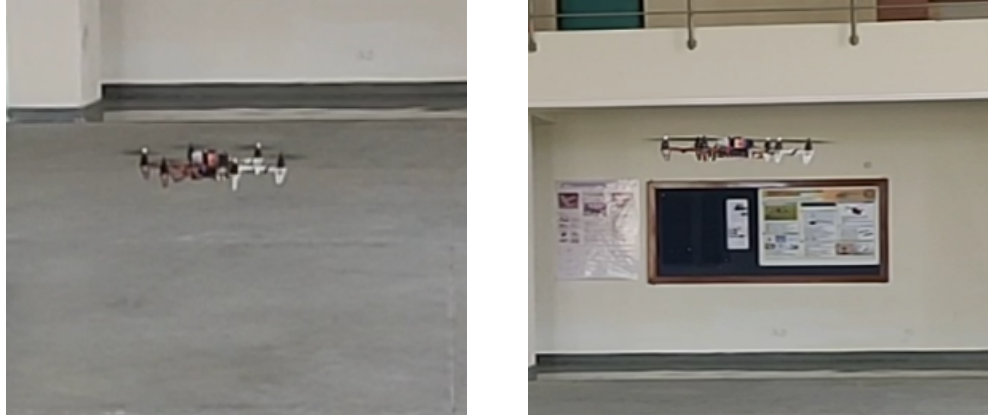


FIGURE 4.23: Conventional hexarotor in hover state.

Experimental validation of the developed lead compensator for the conventional hexarotor is presented in this section. The same module created for attitude control of the conventional quadrotor is used. However, actuator allocation is changed for this case. With the gains for roll and yaw designed in Fig. 3.11 and 3.13, respectively, the closed-loop response is very stable. The hexarotor can be seen in its hover state in Fig. 4.23.

The roll, pitch, and yaw tracking performance during one of the experiments is shown in Fig. 4.24. Highly satisfactory response is observed for all three subsystems.

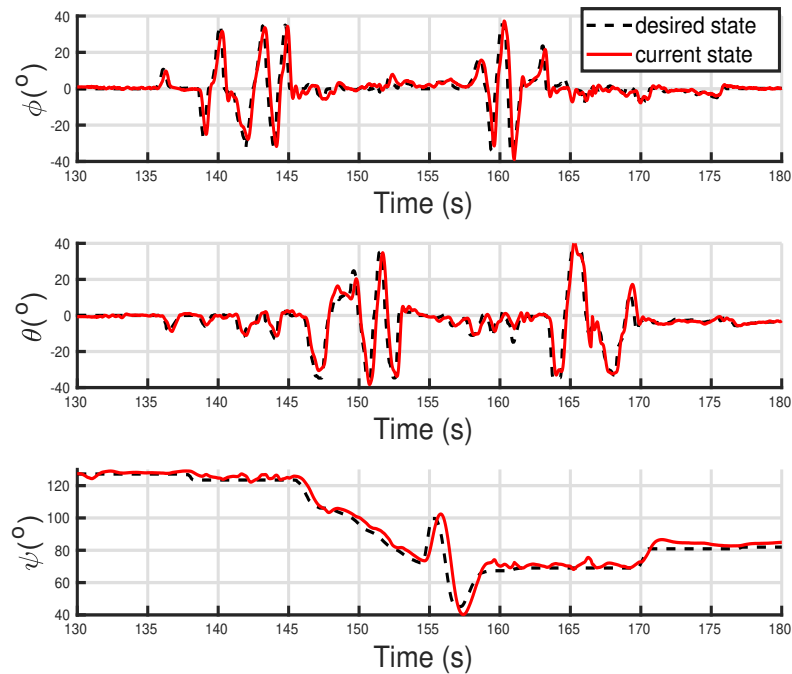
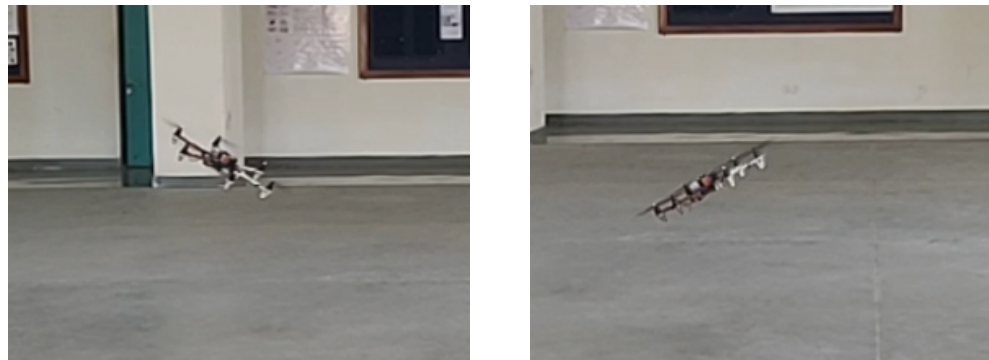


FIGURE 4.24: Roll, pitch, and yaw tracking using the variable-pitch quadrotor in Fig. 1.2 (B). The compensator synthesized in Fig. 3.11 is used for the roll and pitch tracking for this vehicle. The compensator synthesized in Fig. 3.13 is used for yaw subsystem control.



(A) Hexarotor with positive roll angle. (B) Hexarotor on the ground.

FIGURE 4.25: Screen grabs of the conventional hexarotor during test flights.



(A) Hexarotor with a positive pitch angle.  
(B) Hexarotor with a negative pitch angle.

FIGURE 4.26: Screen grabs of the conventional hexarotor performing pitching moment maneuvers.

### 4.2.3 Variable-pitch Quadrotor

Experimental validation of the developed compensator for a variable-pitch quadrotor is shown in this section. Similar to the conventional quadrotor experiments, a new module for attitude control of the novel vehicle is created in the PX4 flight stack. The EKF provides state feedback. A very stable hover is achieved using the designed compensator and can be seen in Fig. 4.27.



FIGURE 4.27: Variable-pitch quadrotor in hover state.

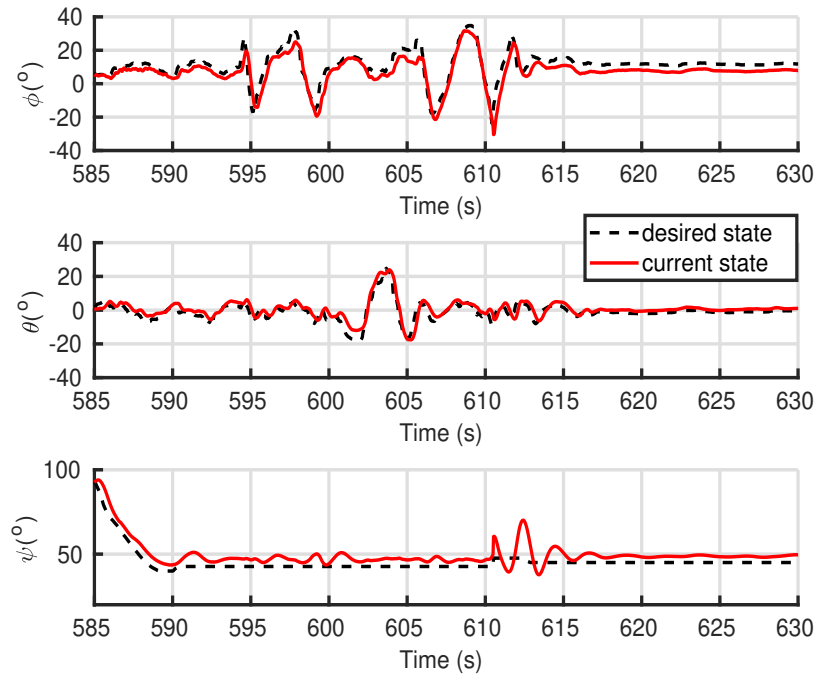


FIGURE 4.28: Roll, pitch, and yaw tracking using the variable-pitch quadrotor in Fig. 1.3. The compensator synthesized in Fig. 3.3 is used for the roll and pitch tracking for this vehicle. The compensator synthesized in Fig. 3.16 is used for yaw subsystem control.

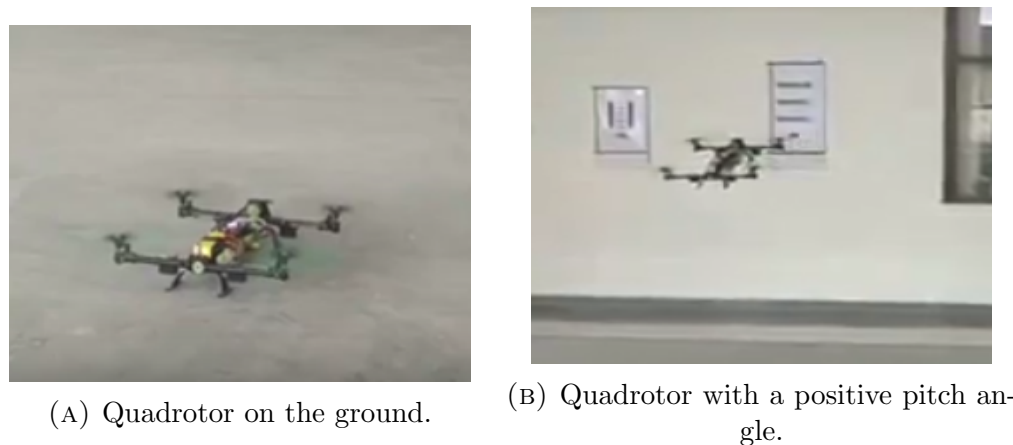


FIGURE 4.29: Screen grabs of the variable-pitch quadrotor during test flights.



(A) Quadrotor with negative roll angle. (B) Quadrotor with positive roll angle.

FIGURE 4.30: Screen grabs of the variable-pitch quadrotor performing negative and positive roll maneuvers.

The tracking response of the variable-pitch quadrotor can be seen in Fig. 4.28. This validates the compensator design given in previous sections. Snapshots of the quadrotor during flights can be seen in Fig. 4.29 and 4.30.

# Chapter 5

## Concluding Remarks

The emergence of UAVs as a viable substitute for tasks that are difficult or dangerous for humans has made it a popular area of research. However, works in existing literature concentrated on developing the vehicle itself with simple control laws with heuristic tuning or on developing complex, nonlinear control laws for aggressive maneuvers restricted to a particular type of vehicle. Looking at the wide range of applications of VTOL UAVs, it would be advantageous to employ a simple generalized control law for the innermost dynamics, i.e., the attitude loop. Since rotorcrafts are in general statically unstable systems, this step cannot be skipped. Once this is stabilized, higher level guidance and control can be achieved.

The purpose of this thesis is to simplify the attitude dynamics and design robust compensators to stabilize and track attitude commands. This has been done through linearization of the attitude dynamics about the hover condition and designing a lead compensator for stabilization. A high phase margin ensures good tracking and minimal overshoot. To further simplify controller tuning, the compensator phase margin for each of the angle subsystems can be tuned using just one parameter. Moreover, this parameter can be obtained analytically as well as through simple MATLAB commands, with only a rough estimate of the rotational inertia of the vehicle. Such a simplistic approach to attitude control allows one to quickly tune and fly any multirotor UAV.

The proposed method is validated through a comprehensive set of numerical simulations as well as experiments. The compensator designed could be used for multiple

types of rotorcraft UAVs by simply changing the only tuning parameter available. Tracking performance is shown to be very good and shows that simplified control design can be deployed for efficient and faster implementations.

# Bibliography

- [1] Airframes reference for px4 flightstack.
- [2] P. Pounds, R. Mahony, and P. Corke. Modelling and control of a large quadrotor robot. *Control Engineering Practice*, 18(7):691–699, 2010.
- [3] Abhijit Das, Kamesh Subbarao, and Frank Lewis. Dynamic inversion with zero-dynamics stabilisation for quadrotor control. *IET control theory & applications*, 3(3):303–314, 2009.
- [4] A. Benallegue, A. Mokhtari, and L. Fridman. Feedback linearization and high order sliding mode observer for a quadrotor uav. *IEEE International Workshop on Variable Structure Systems (VSS)*, pages 365–372, June 2006.
- [5] S. Bouabdallah and R. Siegwart. Full control of a quadrotor. In *2007 IEEE/RSJ International Conference on Intelligent Robots and Systems*, pages 153–158, Oct 2007.
- [6] Tarek Madani and Abdelaziz Benallegue. Backstepping control for a quadrotor helicopter. In *IEEE/RSJ International Conference on Intelligent Robots and Systems*, pages 3255–3260. IEEE, 2006.
- [7] N. Fethalla, M. Saad, H. Michalska, and J. Ghommam. Robust tracking control for a quadrotor uav. In *2017 25th Mediterranean Conference on Control and Automation (MED)*, pages 1269–1274, July 2017.
- [8] B. Wang, L. Mu, and Y. Zhang. Adaptive robust tracking control of quadrotor helicopter with parametric uncertainty and external disturbance. In *2017 International Conference on Unmanned Aircraft Systems (ICUAS)*, pages 402–407, June 2017.

- [9] Z. T. Dydek, A. M. Annaswamy, and E. Lavretsky. Adaptive control of quadrotor uavs: A design trade study with flight evaluations. *IEEE Transactions on Control Systems Technology*, 21(4):1400–1406, July 2013.
- [10] B. Erginer and E. Altug. Modeling and pd control of a quadrotor vtol vehicle. *IEEE Intelligent Vehicles Symposium*, pages 894–899, June 2007.
- [11] Samir Bouabdallah, Andre Noth, and Roland Siegwart. Pid vs lq control techniques applied to an indoor micro quadrotor. In *2004 IEEE/RSJ International Conference on Intelligent Robots and Systems (IROS)*, pages 2451–2456, 2004.
- [12] Mark Cutler, N Kemal Ure, Bernard Michini, and Jonathan P How. Comparison of fixed and variable pitch actuators for agile quadrotors. In *AIAA Guidance, Navigation, and Control Conference (GNC)*, 2011.
- [13] Abhishek, Ram Gadekar, Ankur Duhoon, Mangal Kothari, S. Kadukar, L. Rane, and G. Suryavanshi. Design, development, and closed-loop flight-testing of a single power plant variable pitch quadrotor unmanned air vehicle. In *Proceedings of 73rd American Helicopter Society Annual Forum*, 2017.
- [14] N. Gupta, M. Kothari, and Abhishek. Flight dynamics and nonlinear control design for variable-pitch quadrotors. In *2016 American Control Conference (ACC)*, pages 3150–3155, July 2016.
- [15] S. Bouabdallah, P. Murrieri, and R. Siegwart. Design and control of an indoor micro quadrotor. In *Robotics and Automation, 2004*, volume 5, pages 4393–4398 Vol.5, April 2004.
- [16] DM Henderson. Euler angles, quaternions, and transformation matrices for space shuttle analysis. 1977.
- [17] Gordon J Leishman. *Principles of helicopter aerodynamics with CD extra*. Cambridge university press, 2006.
- [18] A Alaimo, V Artale, C Milazzo, A Ricciardello, and L Trefletti. Mathematical modeling and control of a hexacopter. In *2013 International Conference on Unmanned Aircraft Systems (ICUAS)*, pages 1043–1050. IEEE, 2013.

- [19] Sigurd Skogestad and Ian Postlethwaite. *Multivariable feedback control: analysis and design*, volume 2. Wiley New York, 2007.
- [20] Lorenz Meier, Dominik Honegger, and Marc Pollefeyns. Px4: A node-based multithreaded open source robotics framework for deeply embedded platforms. In *IEEE International Conference on Robotics and Automation (ICRA), 2015*, pages 6235–6240. IEEE, 2015.